Systematic Regional Aerosol Perturbations (SyRAP) in Asia using the intermediate-resolution global climate model FORTE2

Camilla W. Stjern[1], Manoj Joshi[2], Laura J. Wilcox[3], Amee Gollo[3], Bjørn H. Samset[1]

[1] CICERO Center for International Climate Research, Oslo, Norway

[2] University of East Anglia, Norwich, England

[3] National Centre for Atmospheric Science, University of Reading, Reading, England

Abstract

Emissions of anthropogenic aerosols are rapidly changing, in amounts, composition and geographical distribution. In East and South Asia in particular, strong aerosol trends combined with high population densities imply high potential vulnerability to climate change. Improved knowledge of how near-term climate and weather influences these changes is urgently needed, to allow for better-informed adaptation strategies. To understand and decompose the local and remote climate impacts of regional aerosol emission changes, we perform a set of Systematic Regional Aerosol Perturbations (SyRAP) using the reduced-complexity climate model FORTE 2. Absorbing and scattering aerosols are perturbed separately, over East Asia and South Asia, to assess their distinct influences on climate. In this paper, we first present an updated version of FORTE2, which includes treatment of aerosol-cloud interactions. We then document and validate the local responses over a range of parameters, showing for instance that removing emissions of absorbing aerosols over both East Asia and South Asia is projected to cause a local drying, alongside a range of more widespread effects. We find that SyRAP-FORTE2 is able to reproduce the responses to Asian aerosol changes documented in the literature, and that it can help us decompose regional climate impacts of aerosols from the two regions. Finally, we show how SyRAP-FORTE2 has regionally linear responses in temperature and precipitation and can be used as input to emulators and tunable simple climate models, and as a ready-made tool for projecting the local and remote effects of near-term changes in Asian aerosol emissions.

1. Introduction

Aerosol emissions have a wide range of impacts on the climate both near to and far from emission sources, spanning from local changes in surface solar radiation and warming to large-scale modifications of atmospheric circulation patterns and monsoon precipitation (Li et al., 2022; Persad et al., 2023). Anthropogenic aerosols have been found to have an outsized near-term influence on extreme events in recent climate model studies (Samset et al., 2018b). In some regions, anthropogenic aerosol impacts have even been shown to dominate over climate impacts from increasing greenhouse gas emissions. One such region is South and East Asia, which is highly vulnerable to climate risk due to a high population density, rapid industrial development, and severe water stress (Giorgi and Gao, 2018; Wang et al., 2021). The region currently suffers the globe's highest loading of anthropogenic aerosols (Zhang et al., 2012), which have impacted several aspects of Asian climate. Aerosol emission trends have been a key driver of the weakening East and South Asian Summer monsoon, causing widespread summertime drying (Bollasina et al., 2011; Dong et al., 2019; Liu et al., 2017), but have also been linked to increases in extreme precipitation over northwest China (Guo et al., 2022). A significant increase in extreme heat events over China has been moderated by high local anthropogenic aerosol emissions (Chen et al., 2019), which have also contributed significantly to catastrophic floods in southwest China (Fan et al., 2015).

Some Asian regions are projected to have potentially large but highly uncertain trends of aerosol emissions in the future (Samset et al., 2019). The strong links between aerosol emissions and Asian climate indicate that future aerosol emission changes are likely to contribute markedly to climate related risk in many highly populated regions. This poses a great adaptation challenge and underlines the urgent need for improved knowledge about the near-term impacts of changes in aerosol emissions.

While observational studies are crucial, a deeper understanding of the processes and mechanisms under different aerosol emission pathways necessitates the use of numerical climate models. Many modelling studies have looked at regional perturbations of specific anthropogenic aerosols with the aim of characterizing the physical response. However, while there are important, consistent findings across these model studies, the use of different experiment designs can make it difficult to understand the causes of differences in the

results. For instance, regional perturbations of BC over Asia in the Precipitation Driver Response Model Intercomparison Project (PDRMIP, Myhre et al. (2017)), involving a tenfold increase in year 2000 BC concentrations in nine earth system models (ESMs), were found to enhance the low-level monsoon circulation and precipitation (Xie et al., 2020). Dong et al. (2016) use the atmospheric component of HadGEM2-ES and remove all SO_2 emissions over Asia, finding the presence of SO_2 to cause local cooling and a weakening of the East Asian monsoon. Westervelt et al. (2018) performed simulations where they remove BC or SO_4 in different regions, including China and India, and looked at responses compared to a year 2000 control simulation. Their three earth system models all showed a local increase in precipitation from removing SO_4 over China, while the local response to removing BC over India varied between the models. Using IGCM4 – the atmospheric component of FORTE2 – Herbert et al. (2022) simulate removal of BC or SO_4 in China or India compared to present-day concentrations in an otherwise similar setup.

While the examples above show some robust findings across studies, it is difficult to assess whether differences originate from experiment design or from inherent differences in how the models respond to the forcing. In addition to the challenge of different experiment designs, model complexity also varies between studies. In complex models, where more processes and connections are at play, identifying the physical mechanisms behind a given aerosol signal is more challenging than in simpler models where there are fewer processes involved. For that reason, reduced complexity models – such as FORTE2 – are a useful tool for understanding the physical responses we see in ESMs. They also have the added benefit of speed of integration, which allows for more and longer simulations at lower cost. It is critical, however, that all main mechanisms of aerosol-climate interactions are represented. This notably includes the aerosol-cloud interactions (ACI), which was recently assessed to make up 2/3 of the total anthropogenic aerosol radiative forcing over the historical era (Forster, 2021), but which is generally not represented in reduced-complexity climate models (e.g., Nicholls et al., 2021; Nicholls et al., 2020) . Including ACI is also important for capturing the pattern as well as the magnitude of the forcing (Zelinka et al., 2023). In the present study, we therefore update our reduced-complexity model to include a basic representation of ACI.

Using FORTE2, we perform Systematic Regional Aerosol Perturbations (SyRAP) of two different aerosol types (absorbing and scattering) in two different regions (South and East Asia). The linearity of the simulated climate to the strength of the perturbations can readily be tested and, in situations where it holds, the SyRAP simulations can be summed and combined to provide information on climate responses to combinations of aerosol emissions from different regions.

The climate impact of regional aerosol perturbations (e.g., Persad and Caldeira, 2018), perturbations of different aerosol species (e.g., Myhre et al., 2017), and comparisons of purely radiative responses versus aerosol-cloud interactions (e.g., Dong et al., 2019) have all been considered in isolation in earlier work. In the framework of the SyRAP concept, we can analyze the relative importance of each of these elements, as well as how they interact, hopefully providing new insight in the topic of regional aerosol impacts.

In the next section we describe the FORTE2 model, the aerosol input data, and how ACI are emulated in the model. Section 3 describes the details of the SyRAP simulation setups. The climatology of FORTE2 is described in Section 4, including an account of its representation of important Pacific circulation patterns. Finally, in Section 5, we present responses in a selection of variables starting with core responses in temperature, precipitation, clouds and dynamics, an account of FORTE2 ACI impacts, regional linearity of the perturbations and dependence on the climate state. Simulations and the general FORTE2 responses are summarized in Section 6.

2. An updated version of the FORTE2 model, and its aerosol representation

2.1 The FORTE2 Model

FORTE 2.0 (FORTE2) is an intermediate-complexity coupled atmosphere–ocean general circulation model (Blaker et al., 2021) consisting of the Intermediate General Circulation Model 4 (Joshi et al., 2015) and the Modular Ocean Model-Array (Webb, 1996). The atmospheric model has a standard T42 resolution and 35 sigma layers, extending up to 0.1 hPa, while the ocean model has 15 vertical layers going down to 800m depth. The atmospheric model has been used in the past in studies of aerosols over Asia (Herbert et al 2022), and its predecessors have been used to explore climate sensitivity (Forster et al.,

2000), the importance of the semi-direct effect of absorbing aerosols (Cook and Highwood, 2004), climate impacts of explosive volcanic eruptions (Highwood and Stevenson, 2003), and precipitation responses to geoengineering (Ferraro et al., 2014).

2.2 The CAMS reanalysis as aerosol perturbation input data

The global gridded speciated aerosol optical depth and vertical distributions used in SyRAP are based on the Copernicus Atmosphere Monitoring Service (CAMSRA) reanalysis (Inness, 2019; Inness et al., 2019). CAMSRA has an 80km (T255) horizontal resolution and provided data from 2003 to 2021 at the time of writing. CAMSRA uses cycle 42R1 of the IFS, which includes an interactive aerosol scheme (Morcrette et al., 2009). Anthropogenic emissions of black carbon, organic carbon, and sulphur dioxide are taken from the MACCity inventory (Granier et al., 2011) for 2003 to 2010, and Representativie Concentration Pathway (RCP) 8.5 thereafter (Riahi et al., 2011). Biomass burning emissions are from the Global Fire Assimilation System, version 1.2 (GFASv1.2; (Kaiser et al., 2012)). Dust and sea salt emissions are calculated interactively. The reanalysis assimilates aerosol optical depth at 550nm from the Advanced Along-Track Scanning Radiometer (AATSR; (Popp et al., 2016)), and the Moderate Resolution Imaging Spectroradiometer (MODIS) aboard Terra and Aqua (Levy et al., 2013). CAMSRA has smaller biases relative to independent observations than the Monitoring Atmospheric Composition and Climate (MACC) reanalysis and CAMS interim analysis (Xian et al., 2023). For more details of CAMSRA, including key updates compared to previous reanalyses, and an evaluation of the CAMSRA aerosol product compared to previous reanalyses and the Aerosol Robotic NETwork (AERONET; (Holben et al., 1998)), see Inness et al. (2019a).

To produce the SyRAP aerosol perturbations used in the experiments described in Section 3, CAMSRA monthly fields of speciated aerosol optical depth and 3D mass mixing ratios for 2003-2021 are interpolated to T42 resolution, to produce monthly climatologies of total anthropogenic (BC, OC and SO_4), absorbing (BC and OC), and scattering aerosol (SO_4) optical depth at each gridpoint. Aerosols are not transported in FORTE2. The aerosols are vertically uniform from the 2nd lowest model layer (σ, or $p/p_{surface}$ = 0.88 or approximately 950 m above the surface) until a pressure level p_{min}. p_{min} is defined, for each gridbox, from CAMSRA as 850 hPa or the first pressure level where the 2003-2021 mean mixing ratio of BC+OC+SO_4

falls below $5x10^{9}$ kg kg^{-1}, whichever is smaller. Over topography, an additional p_{min} threshold is set such that $\sigma_{min} < 0.75$ and $p_{min} > 300$ hPa. Typical values of p_{min} are 600hPa over much of South Asia and 700hPa over much of East Asia in May. These profiles are then fed into the FORTE2 radiation scheme.

2.3 New Aerosol-cloud-interactions in FORTE2

Aerosol-cloud interactions such as aerosol impacts on cloud albedo or lifetime, are not included in the original setup of FORTE2. However, we include new functionality for SyRAP, used in some of the SO_4 perturbation simulations (Section 3). Within a specified region, ACI is parameterized when aerosol optical depth $\tau > 0.07$. If any of low-level cloud, mid-level cloud, or shallow convective cloud are present, the effective cloud particle radius in those clouds is changed from 15μm to 10μm. (Dong et al., 2019) The $\tau > 0.07$ threshold ensures that ACI forcing does not occur in each gridbox of the specified region, which would be too unrealistic, and gives an ACI distribution in the tropics similar to that seen in CMIP6 models.

A potential caveat in the SyRAP set-up, particularly related to the ACI effect, is the experiment design of a zero-aerosol background. As the susceptibility of clouds to microphysical impacts of aerosols tend to be stronger the cleaner the background (Platnick and Twomey, 1994), this is likely to have some impact on the magnitude of the ACI effects in this study. Note, however, that while this would make the clouds in more complex earth system models including a microphysics scheme extremely susceptible to aerosol perturbations, this is not an issue in the simpler FORTE2, where the magnitude of the ACI effect is designed to be comparable to findings in the literature. Note also that ACI effects are only included in two experiments, as described in the next section. The core experiments in this paper include only aerosol-radiation interactions, which should not be sensitive to the background aerosol level.

3. Systematic Regional Aerosol Perturbations (SyRAP) in FORTE2

3.1 Core SyRAP simulation overview

In the Systematic Regional Aerosol Perturbation (SyRAP) simulations performed here, baseline simulations with no aerosols are compared to perturbation simulations with added

absorbing (black carbon, BC, and organic carbon, OC) or scattering (sulfate, SO_4) aerosols over India and surrounding regions ("IND", coordinates 65°E-95°E, 5°N-35°N) or over parts of East China and surrounding regions ("CHI", coordinates 95°E-133°E, 20°N-53°N). IND and CHI are shown as black dashed and solid boxes, respectively, in Figure 1. Aerosols are perturbed separately in either CHI or IND, or over both regions at once (IND+CHI) – see Table 1 for an overview of the perturbations. The experiments adding BC and OC are labelled "BC" for simplicity.

CORE	**BC** *[AOD of added BC+OC]*	**SO4** *[AOD of added SO4]*	**ACI only**	**SO4 with ACI**	**Climate states**
IND (India) 65:95E, 5:35N	**BC_IND** *[0.010]*	**SO4_IND** *[0.104]*	**---**	**---**	**piC, +1K**
CHI (East China) 95:133E, 20:53N	**BC_CHI** *[0.015]*	**SO4_CHI** *[0.126]*	**---**	**---**	**piC, +1K**
IND+CHI	**BC_IND+CHI**	**SO4_IND+CHI**	**aci_IND+CHI**	**SO4aci_IND+CHI** *Changing effective droplet radius from 15 µm to 10 µm*	**piC, +1K**
LINEARITY TESTS, smaller India region					
NIND (India) 65:95E, 20:35N	BC_NIND	SO4_NIND	---	---	piC
NIND+CHI	BC_NIND+CHI	SO4_NIND+CHI	---	---	piC
ACI SENSITIVITY TEST, done for IND+CHI					
Changing effective droplet radius from 15 µm to 13 µm	---	---	aci_reff13_IND+CHI	SO4aci_reff13_IND+CHI	piC, +1K

Table 1: SyRAP-FORTE simulations performed for the present study. Each indicated simulation was run for 200 years. Core simulations are shown in bold, the rest are linearity or sensitivity tests. "Climate state" refers to the global mean surface temperature change relative to preindustrial conditions. The geographical regions where aerosol optical depth is perturbed are shown in Figure 1.

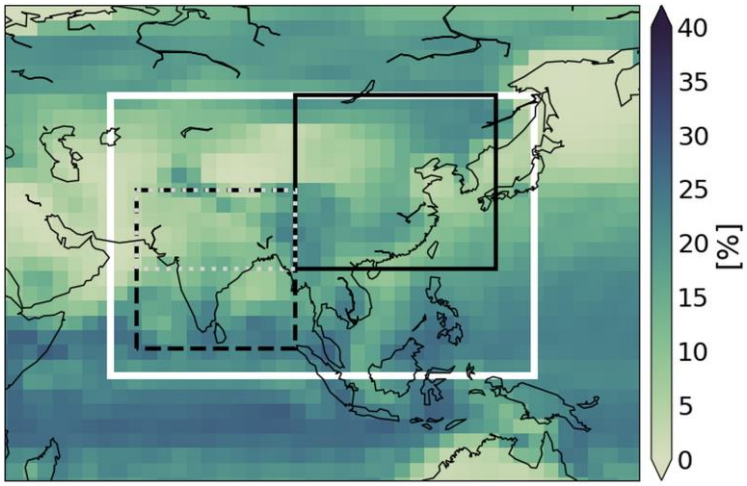

Figure 1: Map showing the region of applied Aerosol Cloud Interactions in white, as well as the India (IND; black, dashed), the smaller North India region (NIND; light grey, dotted) and China (CHI; black, solid) regions, on top of the climatological piC summertime (JJA) convective cloud cover.

The added absorbing (BC and OC) and scattering (SO_4) AODs are shown in Figures 2a and d. The regional mean BC+OC AOD added in the BC_CHI and BC_IND experiments are 0.015 and 0.010, while the regional mean SO4 AOD added in the SO4_CHI and SO4_IND experiments are 0.126 and 0.104. To illustrate the magnitude of these perturbations we show in Fig. 2 the change in surface short wave radiation from adding BC to CHI (panel b) and to IND (panel c). The panels in Fig. 2e and f show corresponding plots for SO_4 but note that these perturbations do not include ACI effects of SO_4. Examples of the impact of the new FORTE2 ACI parameterization will be given in Section 5.2.

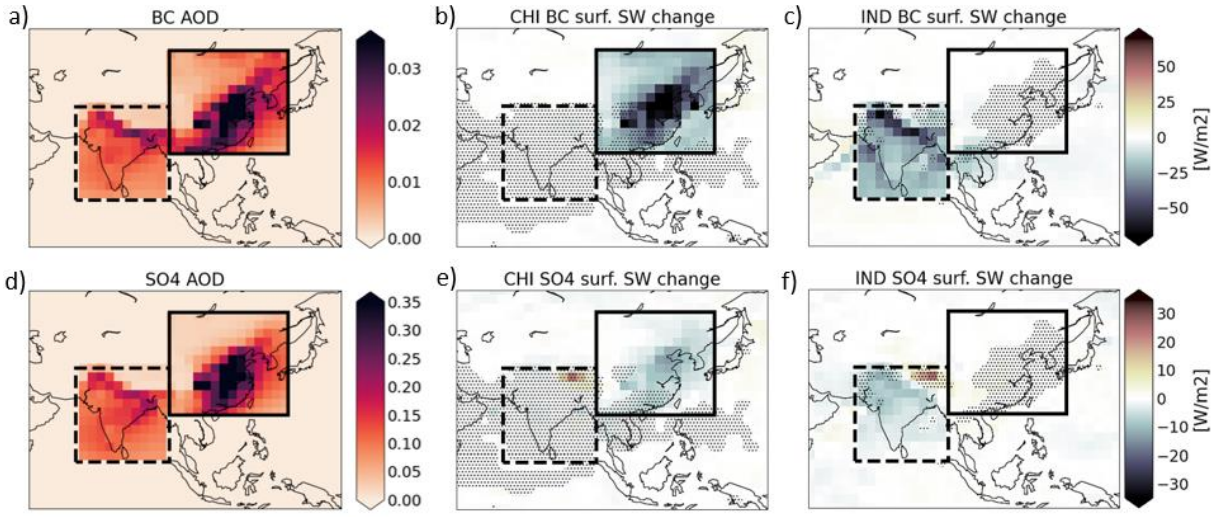

Figure 2: Maps showing the anthropogenic aerosol optical depth (AOD) of a) BC and OC and d) SO_4 within the China (CHI, solid) and the India (IND, dashed) regions, as well as the response in downwelling surface solar radiation to adding the BC/OC to b) CHI and c) IND, and the SO_4 to e) CHI and f) IND, respectively. Grey hatching indicates where responses are not statistically significant.

3.2 ACI implementation

In the SyRAP simulations FORTE2 is for the first time set up with the ability to emulate the indirect aerosol effect – in isolation or in combination with aerosol radiation interactions (ARI). While typically not included in reduced-complexity climate models, aerosol cloud interactions (ACI) account for most of the aerosol forcing globally (Forster, 2021; Zelinka et al., 2014), and there are indications that the ACI is important for the Asian response to aerosol specifically (Dong et al., 2019). The scientific body of evidence points towards dynamical rather than thermodynamical mechanisms dominating the aerosol response over Asia (Tian et al., 2018), making it particularly important to get the total aerosol forcing and its geographical pattern right.

The SyRAP ACI simulations allow us to test how important the ACI is for the simulated response to aerosol forcing in this region. The magnitude and pattern of the ACI effect can be easily changed in the model set-up, by scaling the applied effective radius anomaly and scaling the aerosol optical depth at which cloud changes occur, respectively. This flexibility can be used to provide insight into, for instance, why ESMs differ in their responses to standardised aerosol emission changes. The ACI can be turned on even when the direct aerosol radiative forcing is turned off, so that the effects of nonlinearities when including ACI can be assessed.

Since the ACI effects of aerosol from China and India are hard to disentangle in reality, and as aerosol is not transported in SyRAP, the ACI runs were only done for the experiments perturbing SO_4 in the combined IND+CHI region. For these experiments, ACI is parametized within a box bounded by coordinates 60°E-140°E, 0°N-53°N (see white box in Fig. 1). The region where ACI is prescribed is chosen to capture regions where significant ACI-induced changes in cloud properties were seen in response to regional aerosol perturbations in HadGEM3 (Dong et al., 2019). In that model, the ACI was shown to be important for the local precipitation response, partly by changing the response in the season when the forcing occurs, and partly by preconditioning the SST pattern that governs the response in later seasons.

As shown in Table 1, we simulate the ACI effect on top of the default radiation-only experiment (SO4aci_IND+CHI), but also the ACI-only effect (aci_IND+CHI). In addition, we do

sensitivity tests reducing the magnitude of the ACI by reducing droplet sizes from 15 to 13 µm, as opposed to from 15 to 10 µm in the regular ACI runs. These runs will be discussed in Section 5.2.

3.3 Background climate states

The conditions under which aerosols influence climate are not constant in time. For instance, GHG-induced warming may change cloud distributions and properties, influencing the pattern and magnitude of aerosol forcing, or change the monsoon climatology to which aerosol forcing is being applied, potentially introducing nonlinearities. To understand how aerosol impacts depend on global warming level, we perform all aerosol perturbations in different baseline climates: one with preindustrial CO_2 levels (280 ppmv, piC) and one with approximately present-day CO_2 levels for which climate is about 1 degree warmer (500 ppmv, +1K). We also did a baseline simulation with future CO_2 levels for which climate is about 2 degrees warmer than preindustrial conditions (850 ppmv, +2K). The relatively large CO_2 concentrations in the latter two runs reflect the low climate sensitivity of IGCM4 of 2.1K on doubling CO_2 (Joshi et al., 2015) and subsequent low transient climate response of FORTE2.

In addition to the core experiments, we also perform an additional set of experiments where the IND region is reduced to a much smaller region comprising only the northern parts of India ("NIND", Table 1). This region is marked in light grey dotted lines in Fig. 1. These simulations will be used when addressing the regional additivity of the climate response to the CHI and IND aerosol perturbations, as discussed further in Section 5.3.

All simulations are run for 200 years, enabling studies of radiative responses over a timescale of < 1 year, fast surface ocean responses on timescales of 10-30 years, and slower deeper ocean changes and equilibrium climate responses. All figures in the present analysis show averages for years 51-200, with the first 50 years discarded to let the climate state equilibrate. Climate responses are calculated as the mean response for a perturbation experiment minus the mean response for the corresponding control simulation. For each grid cell, we perform a two-tailed Student's t-test to identify where differences between the control and perturbed simulation are statistically significant at the 5% level. In map plots, we add hatching to areas where changes are *not* statistically significant.

4. FORTE2 climatological characteristics

4.1 Baseline climatology

The climatological distribution of temperature and precipitation in the baseline (piC) simulations are shown in Fig. 3 a) and d), respectively. A thorough evaluation of the preindustrial climatology of FORTE2 was conducted in Blaker et al. (2021). Blaker et al. (2021) show that the model's near-surface air temperature compares well to the NOAA-CIRES-DOE Twentieth Century Reanalysis (20CR), both in terms of averages and seasonal variability. The largest biases are cold temperature anomalies over the polar regions and the Himalayas, and a warm anomaly over the Southern Ocean. FORTE2 simulates too little rainfall compared to the 20CR**,** in particular over the tropical west Pacific, and the South Pacific ITCZ in FORTE2 is too narrow and zonal compared to the reanalysis. While the model performs well in terms of wintertime precipitation over South and East Asia, there is a dry bias in the summer monsoon. Such a bias is typical for the majority of both the CMIP5 and the CMIP6 ensemble (Sperber et al., 2013; Wilcox et al., 2020). The Asian summer monsoon circulation is also too zonal over South East and East Asia, again consistent with the biases seen in CMIP models.

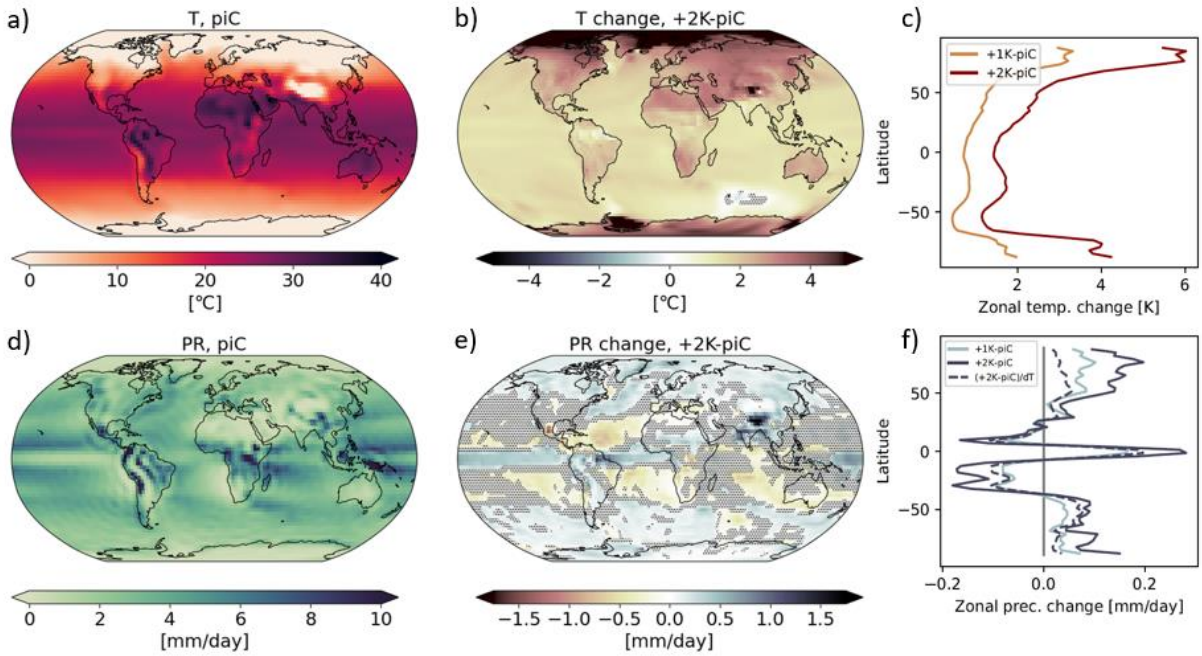

Figure 3: Baseline climatologies (for piC) of annual mean a) temperature (T) and d) precipitation (PR), as well as geographical patterns of b) T and e) PR changes for +2K-piC. Rightmost panels show zonal annual mean changes of c) T and f) PR. Included in the zonal precipitation panel is also the +2K-piC precipitation change divided by the global mean +2K-piC temperature change (dT), illustrating the hydrological sensitivity compared to +1K-piC.

295 The middle panels of Figure 3 show the climatological differences between +2K and piC and
296 illustrate how temperature and precipitation in FORTE2 respond to a strong increase in CO_2.
297 The 2 K global mean surface warming in FORTE2 reproduces known patterns such as an
298 Arctic amplification (Fig. 3b), seen also in the zonal mean temperature changes in Fig. 3c (in
299 the zonal panels we include differences for both +1K-piC and +2K-piC). However, this
300 warming, while causing clear responses in regional precipitation (Fig. 3e), produces a global
301 mean precipitation change of only 0.02 mm/day or 0.64 %. This gives a hydrological
302 sensitivity (HS) of merely 0.32 %/K. In comparison, energy budget constraints dictate a
303 theoretical HS of about 2 %/K (Allen and Ingram, 2002), and the CMIP6 model average HS
304 after 150 years of the 1pctCO2 simulation is 1.6 %/K (Norris et al., 2022). There are two main
305 reasons for the low FORTE2 HS. One is the low climate sensitivity, which means that the
306 relative increase in CO2 per Kelvin of warming is high in this model. This, in turn, means that
307 the long wave absorption from CO2 acts to mute the precipitation increase (Myhre et al.,
308 2018). The other reason is that FORTE2 has a relatively higher fraction of its rain over land,
309 where the HS is markedly lower than the global mean (Samset et al., 2018a). While the HS is
310 low, muting the absolute precipitation response to climate forcings, the overall patterns are
311 still in line with expectations when compared e.g. to CMIP6 (Tebaldi et al., 2021) or PDRMIP
312 (Samset et al., 2016) responses.

313 The dashed line in Fig. 3f shows the +2K-piC precipitation change divided by the +2K-piC
314 global mean temperature difference. As the global mean temperature change between piC
315 and +1K is by definition around 1K, we can compare the dashed and the light blue line to see
316 that the precipitation response in the two climate states (+1K and +2K) is reasonably linear.
317 There are some differences around Southern Hemisphere midlatitudes and at higher
318 Northern Hemisphere latitudes, but the zonal mean precipitation response to warming is
319 very consistent around the latitudes of the region of focus in this study. In Section 5.4 we
320 take a closer look at how aerosol responses may differ when aerosols are added at different
321 global warming levels.

322 The Asian precipitation response to +1K and +2K warming is shown in Fig. 4. In winter, there
323 is little precipitation during the winter monsoon, and the precipitation response to warming
324 is also small. In summer, global warming results in increased precipitation over most of Asia.
325 Note, however, that while Fig. 3f suggested a linear precipitation increase from +1K to +2K,

the geographical patterns in Fig. 4 do not show such linearity over for instance Northeast China. The pattern of the precipitation increase in +2K reflects the climatological precipitation pattern, with the maximum increase located in the region of the maximum precipitation in piC.

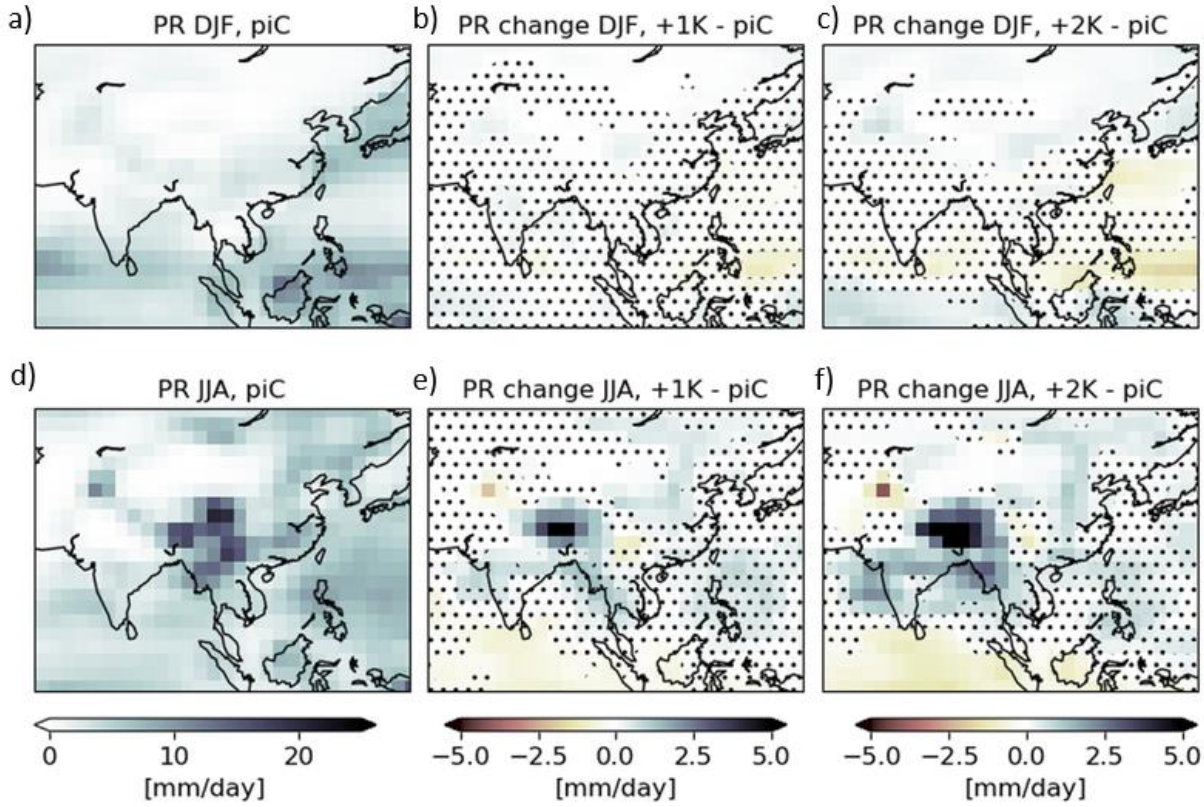

Figure 4: DJF precipitation over Asia for a) piC, b) the difference between piC and +1K, and c) the difference between piC and +2K. Corresponding JJA plots are given in panels d), e) and f), respectively. Maps show averages over simulated years 51-200, and hatching indicates gridcells where the anomalies relative to piC are not significant at the 5% level.

Zooming in on the region of interest in this paper, we show in Fig. 5 climatological (piC) surface pressure and 850 hPa wind for the summer (JJA) and winter (DJF) months, respectively. FORTE2 is compared to ERA5 reanalysis (Hersbach et al., 2020), averaged over the 1940-2022 period. The direction of the monsoon flow over South Asia is well captured by FORTE2. However, the flow is too weak over India and the Bay of Bengal, and is too zonal over Southeast Asia. The zonal flow over Southeast Asia, and an easterly bias in the location of the West North Pacific Subtropical High contribute to a dry bias over northeastern China. Most of the Asian summer monsoon precipitation in FORTE2 falls over Myanmar and

southern China (Fig 4d), while India and northeastern China are too dry. Such dry biases are common in CMIP6 models (Wilcox et al., 2020). However, the atmosphere component of FORTE, IGCM4, has been shown to reproduce the observed seasonal cycle in precipitation well (Herbert et al., 2022).

In winter, the Aleutian low is too weak in FORTE2 compared to ERA5. Combined with a low pressure bias over land, this causes the East Asian Winter Monsoon to also be too weak, although the direction of the flow over northeast Asia is in good agreement with the reanalysis. The seasonal variation in sea level pressure over Asia is small in FORTE2 compared to ERA5, which is largely due to the pressure over land being too high in winter.

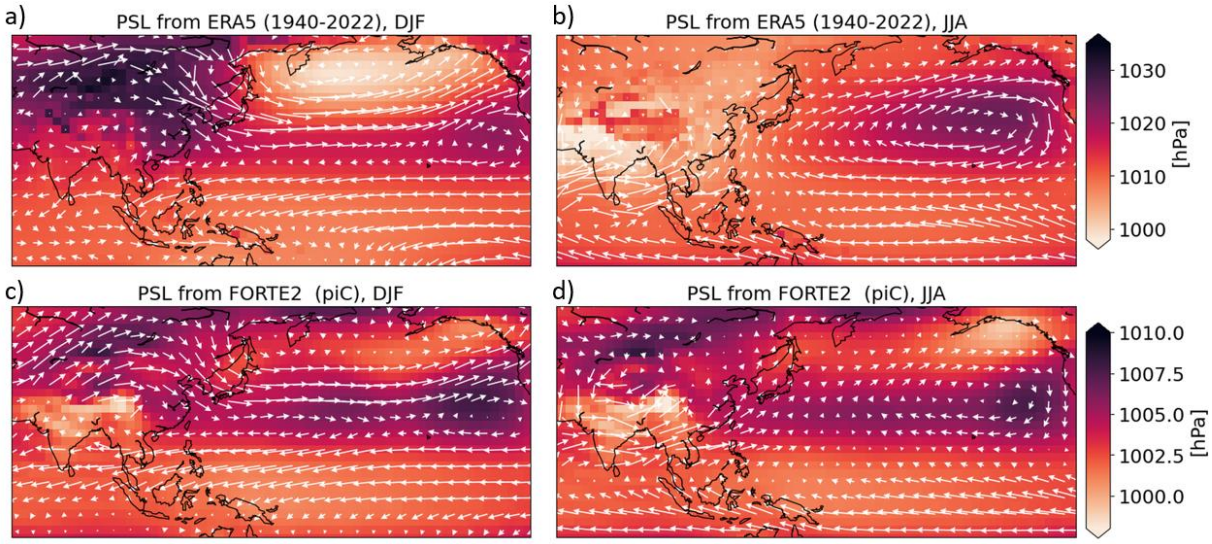

Figure 5: Mean sea level pressure and 850hPa winds (arrows) for ERA5 (averaged over 1940-2022) for DJF (a) and JJA (b), and for FORTE2 piC (years 51-200) for DJF (c) and JJA (c). Note that color scale limits are different between ERA5 and FORTE.

4.2 Pacific Ocean Response

Due to the proximity of the perturbation zones to the Pacific region it is useful to assess the Pacific climatological state across the baseline climates. If differences are found between the baselines (i.e., between piC, +1K and +2K) due to different CO_2 loadings, they are likely to modify the Asian responses to regional aerosol perturbations at the different warming levels, as changes in the Pacific circulation are an important part of the response to Asian aerosol forcing (e.g.,Dong et al., 2019; Wilcox et al., 2019; Williams et al., 2022).

Experiment	Niño 3 Index Standard Deviation	Niño 3.4 Index Standard Deviation	Number of El Niño Events	Number of La Niña Events
piC	0.52	0.59	15	16
+1K	0.53	0.58	17	23
+2K	0.52	0.58	16	21

Table 2: ENSO related statistics including the two commonly used Niño regions and a breakdown of the number and type of ENSO events in the three SyRAP FORTE2 baseline climates.

Standard deviations of the Niño 3.4 index are presented in Table 2 (column three) and remain within a 0.1 tolerance of one another; FORTE2's Nino 3.4 variance is on the weaker end of CMIP6 models, though not an outlier (Chen et al., 2023). ENSO frequency is between 2 and 3 years for each baseline, which is consistent with the observed ENSO occurrence of around once every 2-7 years (Allen, 2000). Table 2 demonstrates that broadly speaking, variability over this key dynamical region is insensitive to changes in the global warming level. Analysis is repeated for the Niño 3 index (column two) and confirms that the Pacific climatological state is insensitive to CO_2 loading.

The large-scale SST patterns and associated winter precipitation anomalies for El Niño and La Niña composites from the piC baseline are presented in Figure 6. This analysis was repeated for the +1K and +2K baselines and the large-scale structures remain consistent across all three baseline climates (not shown). The spatial structures of both El Niño and La Niña SST composites are consistent with events captured in the Extended Reconstructed SST version 3b (ETSSTv3b) reanalysis over the period 1949 to 2015 (see Li et al., 2018). Notable differences are: in the El Niño composite, Fig 6a, the magnitude of SST anomaly is around 30% weaker on the equatorial South American coastline, and in the La Niña composite the cold anomaly extends too far towards the Maritime continent. Anomaly peak strength is weaker than observed, around 35% and 45% weaker for the El Niño and La Niña composites respectively, consistent with Blaker et al. (2021).

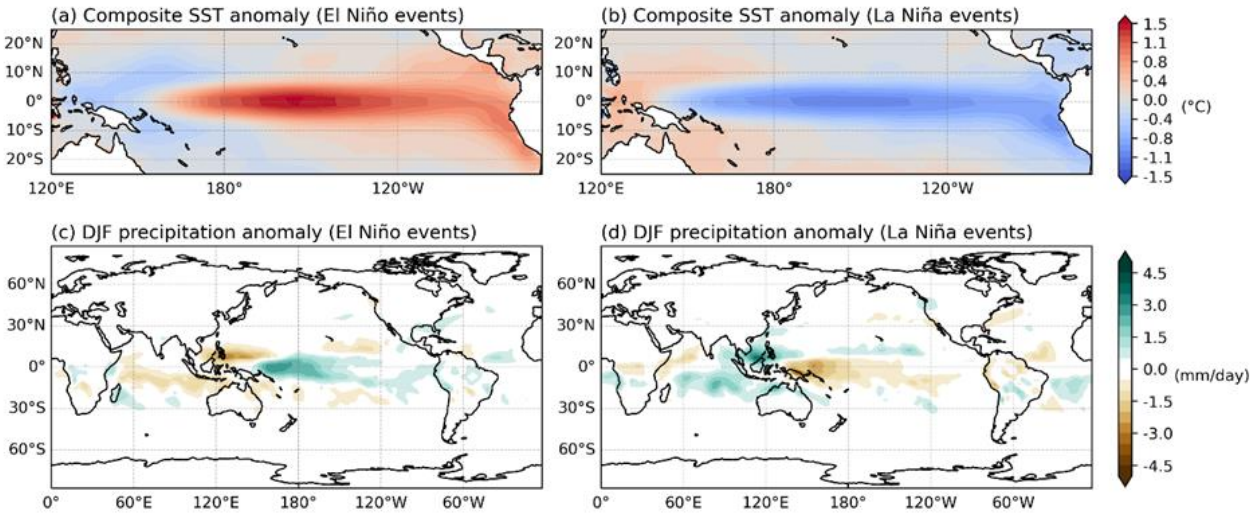

Figure 6: (Top Row) Composite anomalies of monthly sea surface temperature during (a) El Niño and (b) La Niña events. (Bottom Row) Winter, DJF, precipitation anomalies for (c) El Niño and (d) La Niña years. Precipitation anomalies with a magnitude of less than 0.5 mm/day are in white. Data from piC baseline only.

Winter precipitation patterns during ENSO years are consistent with literature (Davey et al., 2014) over the Pacific and maritime continent. Expected remote precipitation impacts, such as a drying signal over southern Africa in El Niño winters (Fig. 6c) and a drying tendency stretching towards India in the La Niña winters (Fig 6d) are captured but are weak. Some remote signals, such as that over Europe, are not captured. FORTE2 is showing some promise in simulating the teleconnections associated with ENSO but this remains an active area for further investigation and model development.

Overall, ENSO events occur with a good frequency but are weaker than observed; particularly La Niña events are short lived and lack strength. ENSO frequency, biases and teleconnections are consistent over all three global warming levels, giving us confidence that any ENSO changes in SyRAP are primarily due to aerosol perturbations, regardless of warming level.

5. Results

5.1 Climate responses to individual aerosol perturbations

In both IND and CHI, the presence of BC causes strong local reductions of up to 75 Wm^{-2} in downwelling surface solar radiation at the surface (Fig. 2b,c). Similar albeit much weaker

reductions are seen for the SO_4 perturbations (Fig. 2e,f). These radiative perturbations trigger thermodynamic responses which manifest as (rapid) changes in near-surface temperature, surface fluxes, precipitation, and clouds, but they also influence the atmospheric circulation patterns in the region, including the Asian Summer Monsoon.

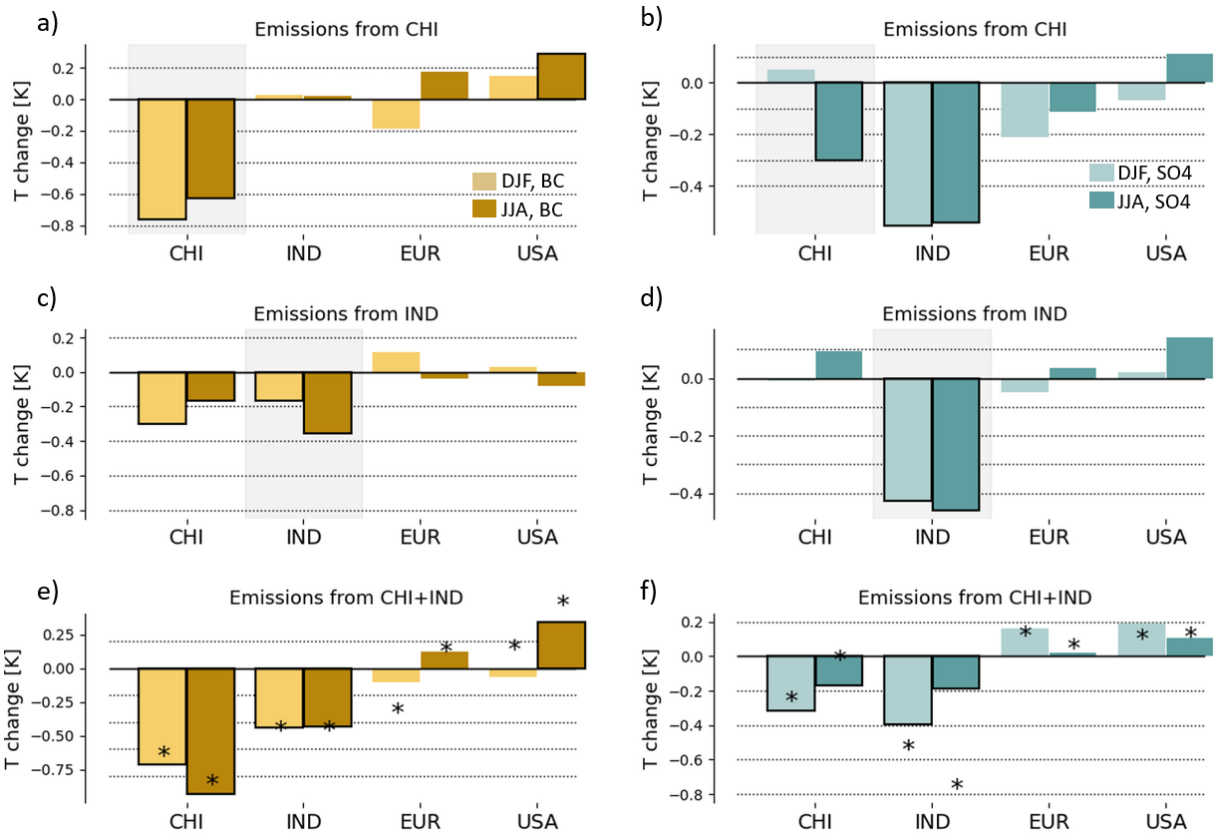

Figure 7: Local (bars shaded by grey area) and remote impacts on regional mean near-surface temperature [K] in the experiments involving adding a) BC to CHI, b) SO_4 to CHI, c) BC to IND, d) SO_4 to IND, e) BC to CHI+IND and f) SO_4 to CHI+IND. Light bars show wintertime (DJF) temperature changes, while dark bars show summertime (JJA) changes. Framed bars indicate where changes are statistically significant, and star symbols in the lowermost row show the summed responses (BC_CHI + BC_IND) or (SO4_CHI + SO4_IND) – responses being linear where bars and stars are comparable in magnitude. We use years 51-200 of the simulation in the analysis.

The dominant local response of adding BC or SO_4 to India or China is a statistically significant cooling (Fig. 7). The only exception is SO_4 emissions over China, which cause insignificant local warming but still trigger a strong cooling effect over India (Fig. 7b). A significant remote effect is also seen for BC over China, which causes significant summertime warming over the USA (Fig. 7a). Regional mean precipitation responses (Fig. S1) are less clear, partly because

the precipitation changes are not uniform in sign across the regional boxes. The regional mean precipitation responses to aerosol predominantly involve local drying, but interestingly SO_4 emissions over China cause significant local summertime precipitation increase over China, but decrease over India. Comparing precipitation responses from the CHI+IND experiment to the all-Asia perturbations of absorbing or scattering aerosols in Herbert et al. (2022), we see that both these studies find a summertime drying over India in response to absorbing aerosols over the larger region. However, while the perturbations cause a significant precipitation increase over China in Herbert et al., we find that Asian absorbing aerosols cause significant drying also over China. Similarly, SO_4 emissions over CHI+IND trigger drying over both regions in FORTE2, while Herbert et al. (2022) find scattering aerosols to cause drying over parts of India but a precipitation increase over China in IGCM4.

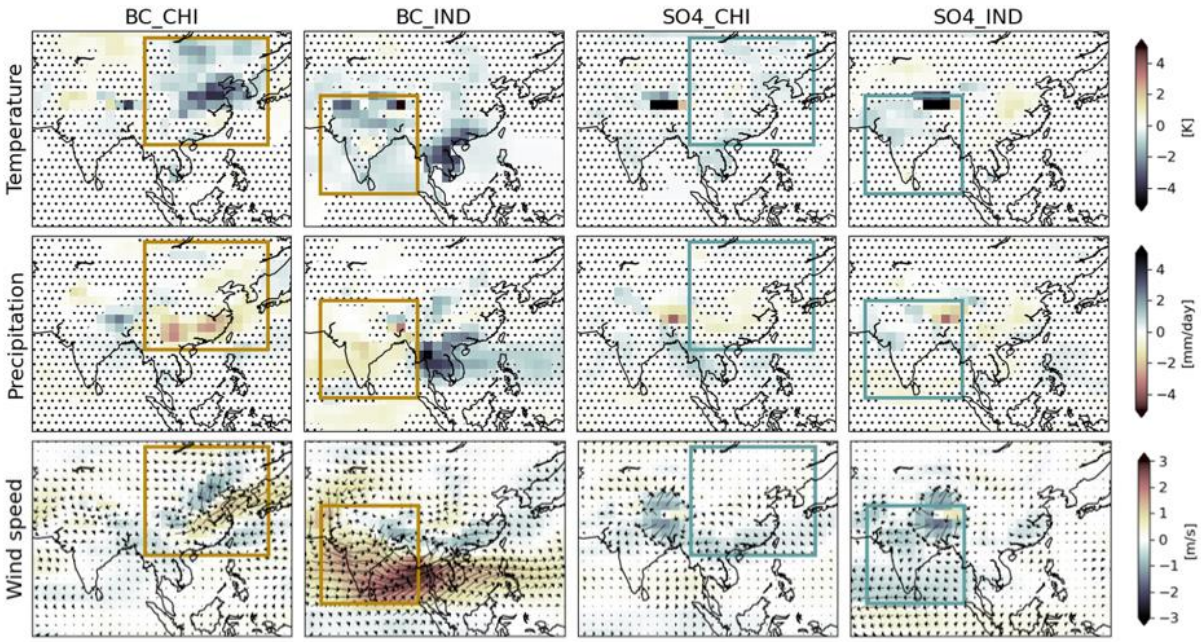

Figure 8: Mean summer (JJA) responses in near-surface temperature, precipitation and 850hPa wind over the Asian region. Solid brown and blue squares mark the region where BC or SO_4 is perturbed, respectively. Maps are based on years 51-200 of the simulations, and hatched regions show areas where differences from the baseline are not statistically significant (by Student's t-test, p-value 0.05).

Figure 8 shows the geographical pattern of the summer (JJA) responses in near-surface temperature, precipitation and wind speed and direction. The addition of BC over China results in near-surface cooling, which is largely located to the north of the Yangtze river

(Figure 8), where the largest reductions in downwelling shortwave radiation at the surface are found (Figure 2). Precipitation south of the Yangtze decreases, associated with a strong reduction in convective cloud there (Figure 9). Adding BC over India also results in a cooling co-located with the change in AOD, but the strongest cooling in this case is seen over southeast Asia, where there is also a large increase in precipitation due to an increase in the strength of the monsoon flow from the Bay of Bengal (Figure 8). However, as in the BC_CHI case, precipitation and convective clouds decrease over the perturbation region due to the combined impact of reduced surface temperatures and increased atmospheric temperatures in response to the absorbing aerosol (see maps of temperature changes at the 850 hPa level in Fig. S2), which has a strong stabilizing effect on the atmosphere.

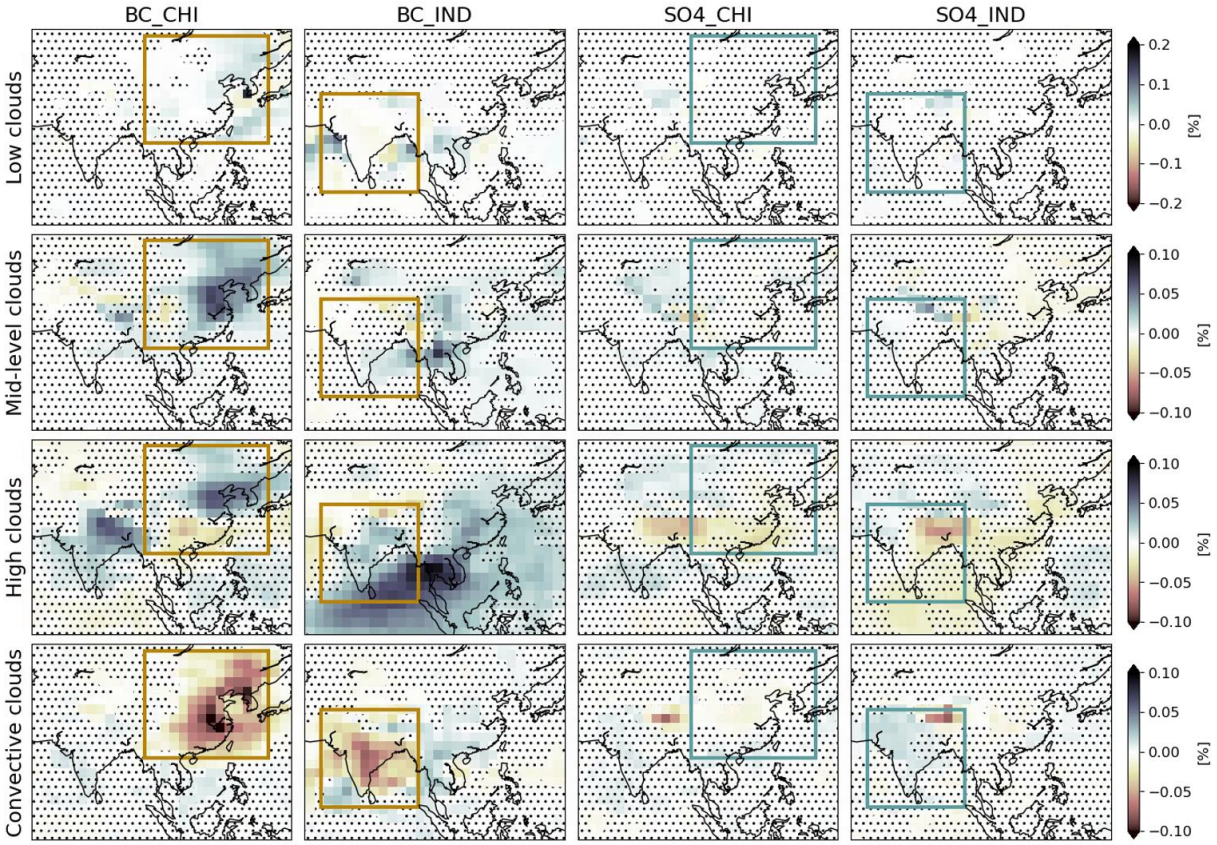

Figure 9: Mean summer (JJA) responses in low, mid-level, high and convective clouds over the Asian region. Solid brown and blue squares mark the region where BC or SO_4 is perturbed, respectively. Maps are based on years 51-200 of the simulations, and hatched regions show areas where differences from the baseline are statistically insignificant (by Student's t-test, p-value 0.05).

The presence of SO_4 also cools the surface, though not as strongly as for BC for the SyRAP perturbations. In SO4_CHI, the cooling is only significant over southeast Asia and northeast Asia. Drying is seen over eastern China, but it is again weaker than in response to BC increases, consistent with a weaker circulation response (Figure 8). Significant cooling is seen in the northwest of the perturbation domain for SO4_IND, co-located with the largest reductions in downwelling shortwave at the surface. This cooling results in a weaker South Asian summer monsoon circulation, and a reduction in precipitation in the northwest of the region (Figure 8). Precipitation and convective cloud increase in the northeast of the perturbation region (Figure 9). Increasing scattering aerosol over South Asia also results in a weakened East Asian summer monsoon, which results in significant warming and drying over eastern China.

Both observations and modelling studies indicate that the drying of the Asian summer monsoon seen over the past decades can be linked to increasing concentrations of anthropogenic aerosols (Li et al., 2015; Liu et al., 2019; Tian et al., 2018). The SyRAP-FORTE2 simulations presented here allow us to decompose and understand contributions from different regions or aerosol species to the total response. As shown in Section 4, FORTE2 reproduces the important features of Asian climate. To confirm that it also has aerosol-driven climate responses consistent with more complex climate models, and thus can be used to explain the decomposition of the response into the main drivers (BC vs. SO_4 or India vs. China), we can compare the responses above to those from earth system model simulations. Note that even among ESMs, the response to aerosol forcing varies strongly between individual models, which means that we do expect there to be some differences between FORTE and other studies.

While most literature on the monsoon response to aerosol focuses on global all anthropogenic aerosol perturbations (Salzmann et al., 2014; Song et al., 2014; Wilcox et al., 2020), some regional aerosol ESM studies exist (see Section 1), for instance based on PDRMIP (Xie et al., 2020; Xie et al., 2022). We find that the Asian JJA precipitation response to combined India and China BC (BC_IND+CHI) is comparable to the multi-model mean MJJAS response of 7 PDRMIP models to a tenfold increase of BC over Asia (Xie et al., 2020). Although set-ups between these two studies are different in many aspects, including different baseline climates (preindustrial versus present-day) and a much stronger

perturbation in the latter case, both FORTE2 and PDRMIP simulations display a BC-induced increase in precipitation over India, although PDRMIP result indicate a drying over Southeast Asia that we do not see. The cooling seen over India in our simulations is found in 8 out of 9 models in the PDRMIP simulations, but the more widespread cooling over East Asia is only seen in a few of the models. Similarly, the impact of regional PDRMIP perturbations of Asian SO_4 on precipitation is studied by Xie et al. (2022), who find a drying of much of the Asian continent but an increase in summer precipitation over arid Central Asia. In FORTE2, the sulfate response is also a drying over much of the region, but the Central Asian JJA precipitation increase extends down to northern India. Recchia and Lucarini (2023) find BC over China to cause local drying but wettening over India and surrounding parts of China, consistent with our findings, as do Krishnamohan et al. (2021) who perform strong BC perturbations in a global climate model and find that local BC enhancement causes a drying over India while BC in China increases India precipitation.

5.2 ACI responses

The new ACI setup allows us to simulate the separate impacts of direct aerosol radiation interactions (ARI) only (the default simulation set-up), the indirect (ACI) effect only, or the simultaneous impact of both effects. Figure 10 shows the impacts of direct and indirect aerosol effects on temperature, precipitation, and SW ERF. The the direct effect of sulfate causes an average (over the ACI region shown in Fig. 1) SW ERF of -1.61 W/m2, while the indirect effect yields a response of -2.16 W/m2, see Table 3. While the direct effect cools most areas over Asia, the indirect effect causes a strong warming over southern parts of India and the region around Thailand (Fig. 10). The contrast between direct and indirect effects of Asian sulfate is particularly stark in the precipitation response (Table 3), and Fig. 10 shows that these differences largely originate in the regions for which the ACI trigger warming.

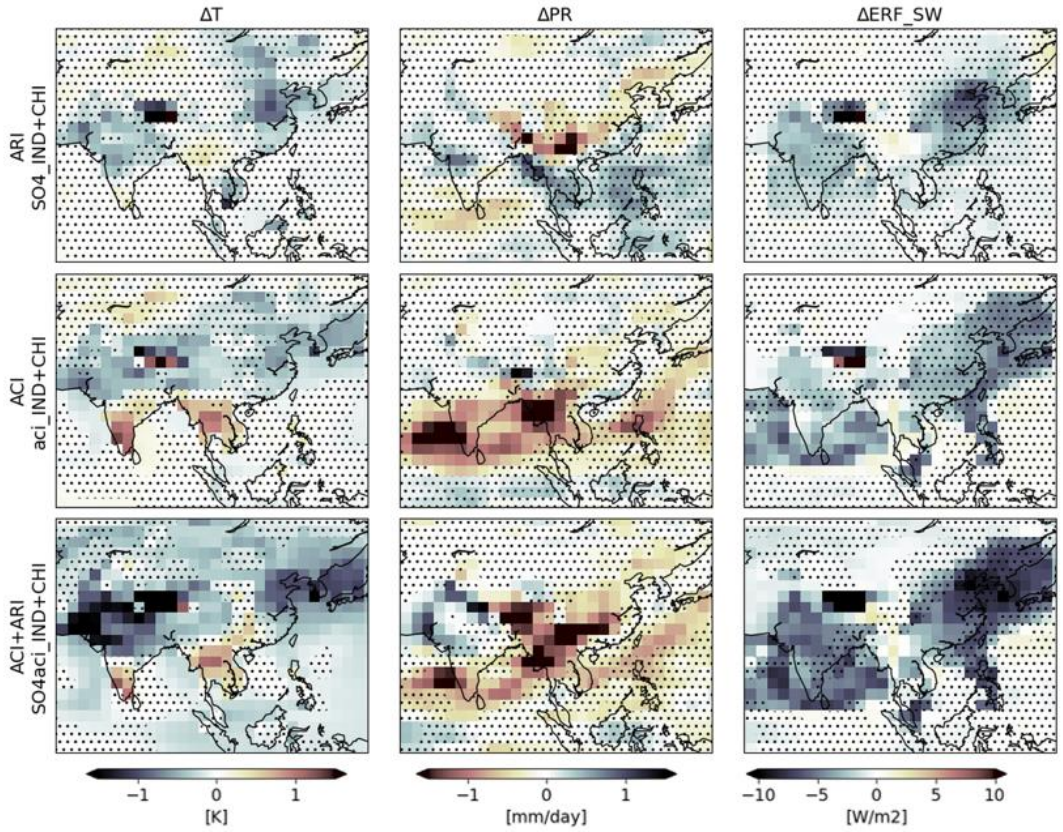

527
528 **Figure 10:** Summer (JJA) response to direct aerosol radiation interactions due to Asian SO4
529 (ARI, top row), as in the default setup in FORTE2, to aerosol-cloud interactions due to Asian
530 SO4 (ACI, middle row) of sulfate as represented, and both the response to Asian SO4
531 including both ARI and ACI (bottom row). Maps are based on years 51-200 of the
532 simulations, and hatched regions show areas where differences from the baseline are
533 statistically insignificant (by Student's t-test, p-value 0.05).

534

	Experiment name	Temp. [K]	Prec. [mm/day]	Surf. SW [W/m2]	ERF_SW [W/m2]
ARI	SO4_IND+CHI	-0.10	0.003	-1.92	-1.61
ACI	aci_IND+CHI	-0.05	-0.30	-2.98	-2.16
(ARI) + (ACI)	SO4_IND+CHI + aci_IND+CHI	-0.15	-0.303	-4.90	-3.77
ARI+ACI	SO4aci_IND+CHI	-0.35	-0.29	-4.79	-4.48
ACI_13um	aci_reff13_IND+CHI	-0.04	-0.06	-1.28	-0.87
ARI+ACI_13um	SO4aci13_reff13_IND+CHI	-0.31	-0.19	-2.73	-2.95

535 **Table 3:** Regional mean JJA impacts of the different ACI simulations, as well as the ARI only
536 simulation (topmost table row). Changes are relative to the piC simulation and are averaged
537 over the ACI region shown in Fig. 1.

Compared to the CMIP5 ensemble (Zelinka et al., 2014), FORTE2 has a similar spatial extent of the ACI-driven SW forcing (see middle panel in rightmost column of Fig. 10). In CMIP5, the maximum negative ACI forcing from scattering aerosols is located a bit north of Indonesia, a pattern that is largely reproduced in FORTE2, albeit with a relatively strong forcing also over Indian land regions. Dong et al. (2019), performing simulations with HadGEM3 with and without the ACI effect, find a much more complex ACI forcing pattern, with positive SW forcing over India and negative over China. In terms of the relative importance of ACI versus ARI, both (Zelinka et al., 2014) and Dong et al. (2019) are consistent with the present study in that ACI exert the strongest radiative impact in the region. Dong et al. (2019) found that ARI resulted in weak circulation and precipitation changes, and that ACI was the dominant driver of monsoon changes. An important part of this mechanism, however, was the ACI-induced warming in Maritime Continent SST, which is not something we see in FORTE2. The precipitation response pattern of Dong et al. (2019) is also very different from FORTE2, with an increase in South Asian and and decrease in East Asian precipitation. The comparison of Guo et al. (2015) showing differences in Asian precipitation patterns between CMIP5 models with and without ACI, however, is more consistent with FORTE2 results. The nine CMIP5 models with only ARI show a drying over China and increased precipitation over India, while the models including ACI give a drying over both India and China, similar to what we find here (Fig. 10).

The clean separation into simulations with ARI-only, ACI-only and both ARI and ACI allows for an assessment of the linearity of these two processes. Looking at the regional means in Table 3, comparing the sum of ARI and ACI (see row "(ARI) + (ACI)") to the experiment including both processes ("ARI+ACI"), we find that while precipitation and downwelling shortwave radiation are close to linear, temperature is not. By closer inspection, this nonlinearity originates from the northernmost latitudes of this region, for which ARI or ACI individually cause warming, but which cools when both ARI and ACI operate simultaneously (Fig. 10). Remote impacts of including the ACI effect, as well as nonlinearities, can be seen in the global maps in Fig. S3. For instance, while both the ARI and ACI effects cause a similar pattern of remote warming over the eastern parts of USA and Canada, the combined impact of these effects does not include such a warming (compare lower two rows of Fig. S3). Likely,

568 the “double” kick to the system is strong enough to trigger a different set of circulation
569 responses including a more unified cooling over the entire North American region.

570 The SyRAP-FORTE2 setup also allows for testing how important the uncertainty in ACI is for
571 the simulated response to aerosol forcing in this region. In the present study, we have tested
572 the sensitivity to the emulated aerosol-induced cloud radius reduction (which in the default
573 setup is reduced from 15 to 10 µm) by performing additional experiments only reducing the
574 droplet radius to 13 µm. Although the relative droplet radius reduction change between
575 default ACI and sensitivity ACI experiments is only 2 µm, the radiative impacts (Surf. SW and
576 ERF_SW in Table 3) are almost halved. Though a large difference, this is not necessarily
577 unrealistic, as the effect on radiation tends not to scale linearly with effective cloud radius
578 (Boers and Rotstayn, 2001). While we also find that the difference in ACI impact on
579 precipitation between these two experiments is substantial, the temperature change is
580 almost the same between the experiments (-0.05 K for the default ACI experiment, and -0.04
581 K for the sensitivity experiment). We also note that the difference in precipitation impacts
582 from ARI+ACI in default versus sensitivity setup is much smaller than when comparing only
583 ACI impacts. Clearly, many nonlinear processes are involved between an initial droplet
584 change, the radiative impact and resulting changes to meteorological variables.

585

586 **5.3 Regional linearity of the perturbations**

587 There are many examples of idealized model simulations of regional aerosol perturbations in
588 the literature, and some of these studies have investigated the regional linearity or additivity
589 of the climate responses. A recent example is Herbert et al. (2022), who used the
590 atmospheric component of FORTE2 and performed separate simulations removing BC or SO_4
591 from India or China. In stark contrast to our results, they find strongly nonlinear responses in
592 the summer monsoon precipitation. Chen et al. (2020) also conclude, after comparing
593 regional climate model simulations adding BC to India, China or both combined, that
594 responses to BC are highly nonlinear. In contrast, Recchia and Lucarini (2023), also using a
595 reduced-complexity model, find relatively linear responses in idealized experiments
596 emulating the addition of BC aerosols over India, China, and Southeast Asia separately or at
597 once.

Here, we investigate the regional linearity in BC/SO_4 perturbations by comparing the added impacts of BC/SO_4 perturbations over IND and CHI to experiments where we perturb BC/SO_4 over both regions at once. The bottom row of Fig. 11 (left half) illustrates the nonlinearity to BC perturbations in the two regions. Positive values mean that adding BC to both regions at once triggers a stronger response than the sum of responses when adding BC to the two regions individually. As indicated by the hatchings in Fig. 11, the regional BC perturbations are significantly nonlinear only in a very small region in Northern India. As can be seen by comparing the individual maps, this region is typically a transitional region between different climate responses. It is also a region of complex topography, and Herbert et al. (2022) showed that different circulation patterns interacting with the orography was a key factor for the nonlinearity of the response.

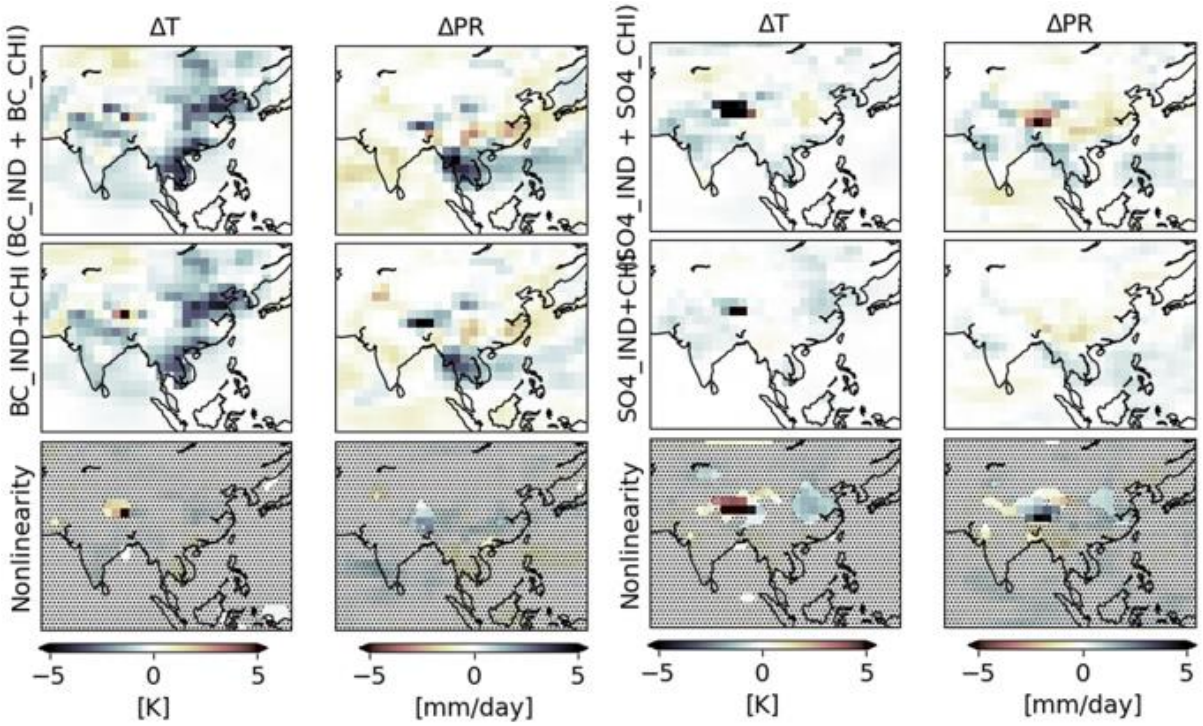

Figure 11: The linearity of mean summer (JJA) temperature and precipitation responses to BC and SO4. Topmost row shows the sum of the responses from the individual regional experiments, middle row show responses from and experiment where aerosol is added to both IND and CHI at once, and bottom row shows the difference between the two above, thus quantifying the nonlinearity. Maps are based on years 51-200 of the simulations, and grid cells with statistically significant nonlinearity are indicated by absence of hatchings.

Nonlinearities in responses to SO_4 (right half of Fig. 11) are slightly larger than for BC. Significant nonlinearities are, like for BC, present over parts of Northern India, but also over China around the same latitudes. In particular, when SO_4 is added to both CHI and IND at

620 once (middle row) there is a small cooling over China not present in the added responses
621 (first row). Looking back at Fig. 8 (upper right corner panel) we see that adding SO_4 to India
622 alone caused a statistically significant warming over China, and this warming is associated
623 with a region of significant anomalous descent (not shown) and reduction in mid-level clouds
624 (Fig. 9). To summarize, some processes are only evident when particularly SO_4 is added to a
625 specific region, and not necessarily when adjacent regions are cooled by SO_4
626 simultaneously. In general, however, responses to both BC and SO_4 in FORTE2 are
627 reasonably linear.

628 As IGCM4 used by Herbert et al. (2022) is FORTE's atmospheric component, their much
629 stronger nonlinearity is surprising. One possible cause of this disparity could be the
630 substantially larger spatial extent of our forcing. To test this, we performed an additional
631 version of the IND experiment where the IND region was limited to the Northern parts of
632 India only, more similar to Herbert et al. (Table 1). Compare black dashed (IND) and light
633 grey dotted line (NIND) in Fig. 1. However, as seen in Figure S4, results are no less linear with
634 this smaller perturbation region. Instead, this discrepancy might arise from the fact that our
635 simulations are fully coupled to an ocean model, or it may be related to the simulation
636 design (for instance, Herbert et al. (2022) remove aerosols from a present-day climate and
637 aerosols field, while we add aerosols to a preindustrial climate with no aerosols). Either way,
638 the linearity allows for the utilization of these simulations in an additive manner.

639 **5.4 Aerosol impacts on Asian climate for different climate states**

640 In the core simulations presented in Section 3, aerosols were perturbed on top of a
641 preindustrial climate (piC) in terms of CO_2 levels (280 ppmv). However, in both the present-
642 day as well as the future, the climate will be in a different state, notably with higher
643 concentrations of CO_2 and higher average temperatures. In a separate set of simulations, we
644 have investigated how the Asian climate responds to BC and SO_4 aerosols on top of a climate
645 that is one degree warmer (+1K; CO_2 level at 500 ppmv) than in our core simulations.
646 Comparing these sets of simulations allows an assessment of whether different climate
647 responses to aerosols can be expected to emerge as climate warms.

648 In general, BC aerosols cause similar geographical precipitation response patterns as climate
649 warms (compare rows in the leftmost half of Fig. 12). The lowermost row indicates that
650 adding BC to China in the different climates does not lead to significant differences in

651 precipitation responses in any widespread subregions, while adding BC to India leads to a
652 significantly weaker precipitation increase over Myanmar and Thailand in the warmer
653 climate.

654

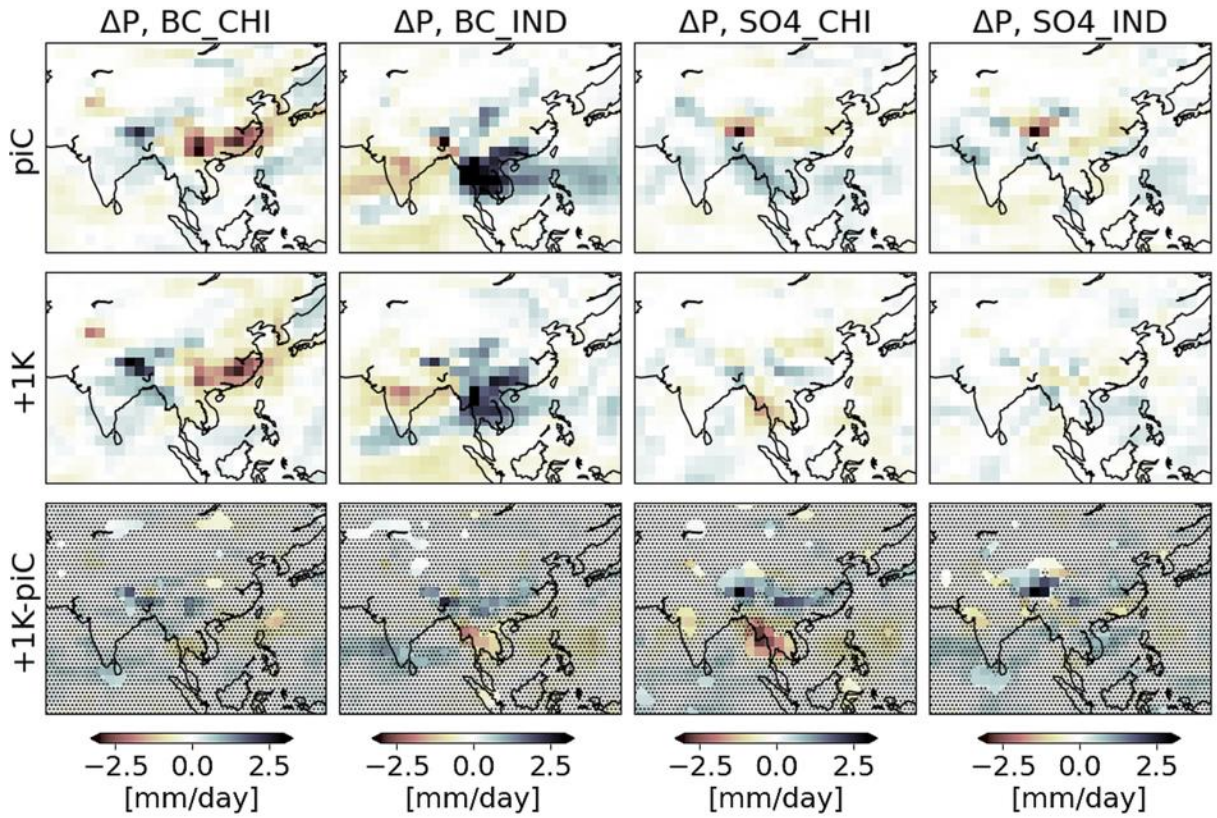

655
656 **Figure 12:** Mean summer (JJA) responses in precipitation in a preindustrial climate (upper
657 row), a 1 degree warmer climate (middle row) and the difference between the two (bottom
658 row). Maps are based on years 51-200 of the simulations, and hatching indicates where the
659 difference between the aerosol responses in the two different climates are not statistically
660 significant.

661

662 In both SO_4 experiments, we see stronger differences in the precipitation response between
663 the different climates. Adding SO_4 over India causes a drying over the Himalayas and the
664 south tip of India in the preindustrial climate but not in the warmer climate. A similar effect
665 in the Himalayan region can be seen for SO_4 over China, but the starkest difference is found
666 over Myanmar and Thailand. In the preindustrial climate the Indian SO_4 triggers a
667 precipitation increase, while in the warmer climate the signal changes sign and becomes a
668 drying. This sensitivity of the SO_4 response to the background climate underlines the
669 importance of the simulation setup when studying aerosol-climate interactions, and also
670 how inferences drawn about sensitivities to aerosol emissions in today's climate may not

hold for future levels of global warming. This remains a largely unquantified source of uncertainty in future projections of aerosol emission influences.

6. Conclusions

Aerosol climate impacts can follow patterns and time evolutions that are different to those from greenhouse gas driven global surface warming, potentially enhancing climate risk when combined with regionally differing socioeconomic factors. However, our understanding of these aerosol specific patterns and processes is still limited. For instance, in Asia, a high population density in combination with high water stress makes the region vulnerable, in particular to changes in precipitation. Recognizing this vulnerability, many previous model studies have analyzed impacts of different types of aerosols from different Asian subregions, studied the role of direct versus indirect aerosol effects, or explored how specific aerosol impacts change in a changing climate.

In this work, using a reduced-complexity climate model, we address all these processes, allowing for a comparison of the relative importance of the different effects. We have shown how a set of systematic aerosol emission perturbations in a reduced-complexity climate model can be used to identify physical responses to regionalized aerosol emissions, with a range of physical properties, and that it is possible to combine these into a tool for building hypotheses about the joint influence of baskets of aerosol emission types.

We found that perturbations of absorbing or scattering aerosols in FORTE2 reproduce important features already shown in the literature, based on observations, and on simulations using more complex earth system models. We find that the presence of black carbon (BC) and sulfate (SO_4) aerosols in China and India cause local reductions in surface solar radiation that trigger thermodynamic responses, leading to changes in temperature, surface fluxes and precipitation. The dynamical responses in pressure, winds, and circulation patterns contribute to changes in clouds and precipitation and have widespread impacts outside the perturbed areas. Adding BC over China causes a strong local precipitation reduction. BC over India also causes local drying but a strong increase in precipitation over Southeast Asia. Adding SO_4 over China leads to reduced precipitation locally, while SO_4 over

India leads to increased precipitation in northwestern India and warming and drying over East China.

The same amount of BC or SO_4 aerosols cause weaker near-surface cooling and precipitation changes in a warmer climate. However, the geographical distribution of precipitation changes on a sub-regional scale reveal important differences. For instance, SO_4 over China causes increased precipitation over Southeast Asia in a preindustrial climate, but in a warmer climate, the precipitation impact of SO_4 on this region changes sign entirely.

Adding the separate response to a given aerosol impact in the two different regions (IND and CHI) are comparable to the impact of adding aerosols to both regions at once. In other words, responses are reasonably linear, which makes the SyRAP simulations well suited as a tool for understanding joint influences of multiple aerosol-driven climate forcings. While the focus of our work has been on Asia, and the regions home to the current dominant emitters of anthropogenic aerosols, similar studies for other regions would be highly useful as a future exercise. They could also include the responses to natural aerosol sources such as dust, biomass burning and sea salt, expected to become more important as we transition into a post-fossil future with a warmer global climate.

Acknowledgements

We acknowledge the Center for Advanced Study in Oslo, Norway that funded and hosted our HETCLIF centre during the academic year of 2023/24. The research presented in this paper was carried out on the high-performance computing cluster supported by the Research and Specialist Computing Support service at the University of East Anglia, UK. Data were stored and shared on project account NS9042KK on resources provided by UNINETT Sigma2 – the National Infrastructure for High Performance Computing and Data Storage in Norway. All coauthors were supported by the Research Council of Norway [Grant no. 324182 (CA^3THY)].

Data availability statement

The present analyses is based on model simulations using the FORTE2 (version v2.0) reduced-complexity climate model . The model is freely available for download at https://zenodo.org/records/3632569. Aerosol perturbation simulations use aerosol optical depth from the CAMSRA, as detailed in the Methods section. The Copernicus Atmosphere Monitoring Reanalysis (CAMSRA) was downloaded from the Copernicus Atmosphere Monitoring Service (CAMS) Atmosphere Data Store (ADS) https://ads.atmosphere.copernicus.eu/cdsapp#!/dataset/cams-global-reanalysis-eac4?tab=overview. Figure 5 compares FORTE2 sea level pressure and winds to that from ERA5 reanalysis (Hersbach et al., 2020), which is available for download here:

https://cds.climate.copernicus.eu/cdsapp#!/dataset/reanalysis-era5-single-levels?tab=overview. All FORTE2 model results are available for download at the repository https://archive.sigma2.no/, at https://archive.norstore.no/pages/public/datasetDetail.jsf?id=10.11582/2023.00140 [data are currently awaiting a DOI and will be available at https://doi.org/xxxx]. Python code for analysis of the FORTE2 results as well as for plotting figures in the manuscript will be available for download at the same repository.

References

Allen, M. R., and Ingram, W. J.: Constraints on future changes in climate and the hydrologic cycle, Nature, 419, 228-232, 10.1038/nature01092, 2002.

Allen, R. J.: ENSO: Multiscale Variability and Global and Regional Impacts, Cambridge Univ. Press, New York, 2000.

Blaker, A. T., Joshi, M., Sinha, B., Stevens, D. P., Smith, R. S., and Hirschi, J. J. M.: FORTE 2.0: a fast, parallel and flexible coupled climate model, Geosci. Model Dev., 14, 275-293, 10.5194/gmd-14-275-2021, 2021.

Boers, R., and Rotstayn, L. D.: Possible links between cloud optical depth and effective radius in remote sensing observations, Quarterly Journal of the Royal Meteorological Society, 127, 2367-2383, https://doi.org/10.1002/qj.49712757709, 2001.

Bollasina, M. A., Ming, Y., and Ramaswamy, V.: Anthropogenic Aerosols and the Weakening of the South Asian Summer Monsoon, Science, 334, 502-505, doi:10.1126/science.1204994, 2011.

Chen, H., Zhuang, B., Liu, J., Li, S., Wang, T., Xie, X., Xie, M., Li, M., and Zhao, M.: Regional Climate Responses in East Asia to the Black Carbon Aerosol Direct Effects from India and China in Summer, Journal of Climate, 33, 9783-9800, https://doi.org/10.1175/JCLI-D-19-0706.1, 2020.

Chen, S., Chen, W., Yu, B., and Wu, R.: How Well Can Current Climate Models Simulate the Connection of the Early Spring Aleutian Low to the Following Winter ENSO?, Journal of Climate, 36, 603-624, https://doi.org/10.1175/JCLI-D-22-0323.1, 2023.

Chen, W., Dong, B., Wilcox, L., Luo, F., Dunstone, N., and Highwood, E. J.: Attribution of Recent Trends in Temperature Extremes over China: Role of Changes in Anthropogenic Aerosol Emissions over Asia, Journal of Climate, 32, 7539-7560, 10.1175/jcli-d-18-0777.1, 2019.

Cook, J., and Highwood, E. J.: Climate response to tropospheric absorbing aerosols in an intermediate general-circulation model, Quarterly Journal of the Royal Meteorological Society, 130, 175-191, https://doi.org/10.1256/qj.03.64, 2004.

Davey, M. K., Brookshaw, A., and Ineson, S.: The probability of the impact of ENSO on precipitation and near-surface temperature, Climate Risk Management, 1, 5-24, https://doi.org/10.1016/j.crm.2013.12.002, 2014.

Dong, B., Sutton, R. T., Highwood, E. J., and Wilcox, L. J.: Preferred response of the East Asian summer monsoon to local and non-local anthropogenic sulphur dioxide emissions, Climate Dynamics, 46, 1733-1751, 10.1007/s00382-015-2671-5, 2016.

Dong, B., Wilcox, L. J., Highwood, E. J., and Sutton, R. T.: Impacts of recent decadal changes in Asian aerosols on the East Asian summer monsoon: roles of aerosol–radiation and aerosol–cloud interactions, Climate Dynamics, 53, 3235-3256, 10.1007/s00382-019-04698-0, 2019.

Fan, J., Rosenfeld, D., Yang, Y., Zhao, C., Leung, L. R., and Li, Z.: Substantial contribution of anthropogenic air pollution to catastrophic floods in Southwest China, Geophysical Research Letters, 42, 6066-6075, https://doi.org/10.1002/2015GL064479, 2015.

Ferraro, A. J., Highwood, E. J., and Charlton-Perez, A. J.: Weakened tropical circulation and reduced precipitation in response to geoengineering, Environmental Research Letters, 9, 014001, 10.1088/1748-9326/9/1/014001, 2014.

Forster, P., T. Storelvmo, K. Armour, W. Collins, J.-L. Dufresne, D. Frame, D.J. Lunt, T. Mauritsen, M.D. Palmer, M. Watanabe, M. Wild, and H. Zhang: The Earth's Energy Budget, Climate Feedbacks, and Climate Sensitivity. , in: The Physical Science Basis. Contribution of Working Group I to the Sixth Assessment Report of the Intergovernmental Panel on Climate Change, edited by: Masson-Delmotte, V., P. Zhai, A. Pirani, S.L. Connors, C. Péan, S. Berger, N. Caud, Y. Chen, L. Goldfarb, M.I. Gomis, M. Huang, K. Leitzell, E. Lonnoy, J.B.R. Matthews, T.K. Maycock, T. Waterfield, O. Yelekçi, R. Yu, and B. Zhou, Cambridge University Press, Cambridge, United Kingdom and New York, NY, USA, pp. 923–1054, 2021.

Forster, P. M., Blackburn, M., Glover, R., and Shine, K. P.: An examination of climate sensitivity for idealised climate change experiments in an intermediate general circulation model, Climate Dynamics, 16, 833-849, 10.1007/s003820000083, 2000.

Giorgi, F., and Gao, X.-J.: Regional earth system modeling: review and future directions, Atmospheric and Oceanic Science Letters, 11, 189-197, 10.1080/16742834.2018.1452520, 2018.

Granier, C., Bessagnet, B., Bond, T., D'Angiola, A., Denier van der Gon, H., Frost, G. J., Heil, A., Kaiser, J. W., Kinne, S., Klimont, Z., Kloster, S., Lamarque, J.-F., Liousse, C., Masui, T., Meleux, F., Mieville, A., Ohara, T., Raut, J.-C., Riahi, K., Schultz, M. G., Smith, S. J., Thompson, A., van Aardenne, J., van der Werf, G. R., and van Vuuren, D. P.: Evolution of anthropogenic and biomass burning emissions of air pollutants at global and regional scales during the 1980–2010 period, Climatic Change, 109, 163, 10.1007/s10584-011-0154-1, 2011.

Guo, L., Turner, A. G., and Highwood, E. J.: Impacts of 20th century aerosol emissions on the South Asian monsoon in the CMIP5 models, Atmos. Chem. Phys., 15, 6367-6378, 10.5194/acp-15-6367-2015, 2015.

Guo, Y., Dong, B., and Zhu, J.: Anthropogenic impacts on changes in summer extreme precipitation over China during 1961–2014: roles of greenhouse gases and anthropogenic aerosols, Climate Dynamics, 10.1007/s00382-022-06453-4, 2022.

Herbert, R., Wilcox, L. J., Joshi, M., Highwood, E., and Frame, D.: Nonlinear response of Asian summer monsoon precipitation to emission reductions in South and East Asia, Environmental Research Letters, 17, 014005, 10.1088/1748-9326/ac3b19, 2022.

Hersbach, H., Bell, B., Berrisford, P., Hirahara, S., Horányi, A., Muñoz-Sabater, J., Nicolas, J., Peubey, C., Radu, R., Schepers, D., Simmons, A., Soci, C., Abdalla, S., Abellan, X., Balsamo, G., Bechtold, P., Biavati, G., Bidlot, J., Bonavita, M., De Chiara, G., Dahlgren, P., Dee, D., Diamantakis, M., Dragani, R., Flemming, J., Forbes, R., Fuentes, M., Geer, A., Haimberger, L., Healy, S., Hogan, R. J., Hólm, E., Janisková, M., Keeley, S., Laloyaux, P., Lopez, P., Lupu, C., Radnoti, G., de Rosnay, P., Rozum, I., Vamborg, F., Villaume, S., and Thépaut, J.-N.: The ERA5 global reanalysis, Quarterly Journal of the Royal Meteorological Society, 146, 1999-2049, https://doi.org/10.1002/qj.3803, 2020.

Highwood, E. J., and Stevenson, D. S.: Atmospheric impact of the 1783–1784 Laki Eruption: Part II Climatic effect of sulphate aerosol, Atmos. Chem. Phys., 3, 1177-1189, 10.5194/acp-3-1177-2003, 2003.

Holben, B. N., Eck, T. F., Slutsker, I., Tanré, D., Buis, J. P., Setzer, A., Vermote, E., Reagan, J. A., Kaufman, Y. J., Nakajima, T., Lavenu, F., Jankowiak, I., and Smirnov, A.: AERONET—A Federated Instrument Network and Data Archive for Aerosol Characterization, Remote Sensing of Environment, 66, 1-16, https://doi.org/10.1016/S0034-4257(98)00031-5, 1998.

Inness, A., Ades, M., Agustí-Panareda, A., Barré, J., Benedictow, A., Blechschmidt, A. M., Dominguez, J. J., Engelen, R., Eskes, H., Flemming, J., Huijnen, V., Jones, L., Kipling, Z., Massart, S., Parrington, M., Peuch, V. H., Razinger, M., Remy, S., Schulz, M., and Suttie, M.: The CAMS reanalysis of atmospheric composition, Atmos. Chem. Phys., 19, 3515-3556, 10.5194/acp-19-3515-2019, 2019.

CAMS global reanalysis (EAC4) monthly averaged fields.: https://ads.atmosphere.copernicus.eu/cdsapp#!/dataset/cams-global-reanalysis-eac4-monthly?tab=overview, 2019.

Joshi, M., Stringer, M., van der Wiel, K., O'Callaghan, A., and Fueglistaler, S.: IGCM4: a fast, parallel and flexible intermediate climate model, Geosci. Model Dev., 8, 1157-1167, 10.5194/gmd-8-1157-2015, 2015.
Kaiser, J. W., Heil, A., Andreae, M. O., Benedetti, A., Chubarova, N., Jones, L., Morcrette, J. J., Razinger, M., Schultz, M. G., Suttie, M., and van der Werf, G. R.: Biomass burning emissions estimated with a global fire assimilation system based on observed fire radiative power, Biogeosciences, 9, 527-554, 10.5194/bg-9-527-2012, 2012.
Krishnamohan, K. S., Modak, A., and Bala, G.: Effects of local and remote black carbon aerosols on summer monsoon precipitation over India, Environmental Research Communications, 3, 081003, 10.1088/2515-7620/ac18d1, 2021.
Levy, R. C., Mattoo, S., Munchak, L. A., Remer, L. A., Sayer, A. M., Patadia, F., and Hsu, N. C.: The Collection 6 MODIS aerosol products over land and ocean, Atmos. Meas. Tech., 6, 2989-3034, 10.5194/amt-6-2989-2013, 2013.
Li, B., Ding, R., Li, J., Xu, Y., and Li, J.: Asymmetric Response of Predictability of East Asian Summer Monsoon to ENSO, SOLA, 14, 52-56, 10.2151/sola.2018-009, 2018.
Li, J., Carlson, B. E., Yung, Y. L., Lv, D., Hansen, J., Penner, J. E., Liao, H., Ramaswamy, V., Kahn, R. A., Zhang, P., Dubovik, O., Ding, A., Lacis, A. A., Zhang, L., and Dong, Y.: Scattering and absorbing aerosols in the climate system, Nature Reviews Earth & Environment, 3, 363-379, 10.1038/s43017-022-00296-7, 2022.
Li, X., Ting, M., Li, C., and Henderson, N.: Mechanisms of Asian Summer Monsoon Changes in Response to Anthropogenic Forcing in CMIP5 Models, Journal of Climate, 28, 4107-4125, https://doi.org/10.1175/JCLI-D-14-00559.1, 2015.
Liu, J., Rühland, K. M., Chen, J., Xu, Y., Chen, S., Chen, Q., Huang, W., Xu, Q., Chen, F., and Smol, J. P.: Aerosol-weakened summer monsoons decrease lake fertilization on the Chinese Loess Plateau, Nature Climate Change, 7, 190-194, 10.1038/nclimate3220, 2017.
Liu, Y., Cai, W., Sun, C., Song, H., Cobb, K. M., Li, J., Leavitt, S. W., Wu, L., Cai, Q., Liu, R., Ng, B., Cherubini, P., Büntgen, U., Song, Y., Wang, G., Lei, Y., Yan, L., Li, Q., Ma, Y., Fang, C., Sun, J., Li, X., Chen, D., and Linderholm, H. W.: Anthropogenic Aerosols Cause Recent Pronounced Weakening of Asian Summer Monsoon Relative to Last Four Centuries, Geophysical Research Letters, 46, 5469-5479, https://doi.org/10.1029/2019GL082497, 2019.
Myhre, G., Forster, P. M., Samset, B. H., Hodnebrog, Ø., Sillmann, J., Aalbergsjø, S. G., Andrews, T., Boucher, O., Faluvegi, G., Fläschner, D., Kasoar, M., Kharin, V., Kirkevåg, A., Lamarque, J.-F., Olivié, D., Richardson, T., Shindell, D., Shine, K. P., Stjern, C. W., Takemura, T., Voulgarakis, A., and Zwiers, F.: PDRMIP: A Precipitation Driver and Response Model Intercomparison Project, Protocol and preliminary results, Bulletin of the American Meteorological Society, 98, 1185-1198, doi: 10.1175/BAMS-D-16-0019.1, 2017.
Myhre, G., Kramer, R. J., Smith, C. J., Hodnebrog, Ø., Forster, P., Soden, B. J., Samset, B. H., Stjern, C. W., Andrews, T., Boucher, O., Faluvegi, G., Fläschner, D., Kasoar, M., Kirkevåg, A., Lamarque, J.-F., Olivié, D., Richardson, T., Shindell, D., Stier, P., Takemura, T., Voulgarakis, A., and Watson-Parris, D.: Quantifying the Importance of Rapid Adjustments for Global Precipitation Changes, Geophysical Research Letters, 45, 11,399-311,405, https://doi.org/10.1029/2018GL079474, 2018.
Nicholls, Z., Meinshausen, M., Lewis, J., Corradi, M. R., Dorheim, K., Gasser, T., Gieseke, R., Hope, A. P., Leach, N. J., McBride, L. A., Quilcaille, Y., Rogelj, J., Salawitch, R. J., Samset, B. H., Sandstad, M., Shiklomanov, A., Skeie, R. B., Smith, C. J., Smith, S. J., Su, X., Tsutsui, J., Vega-Westhoff, B., and Woodard, D. L.: Reduced Complexity Model Intercomparison Project Phase 2: Synthesizing Earth System Knowledge for Probabilistic Climate Projections, Earth's Future, 9, e2020EF001900, https://doi.org/10.1029/2020EF001900, 2021.
Nicholls, Z. R. J., Meinshausen, M., Lewis, J., Gieseke, R., Dommenget, D., Dorheim, K., Fan, C. S., Fuglestvedt, J. S., Gasser, T., Golüke, U., Goodwin, P., Hartin, C., Hope, A. P., Kriegler, E., Leach, N. J., Marchegiani, D., McBride, L. A., Quilcaille, Y., Rogelj, J., Salawitch, R. J., Samset, B. H., Sandstad, M., Shiklomanov, A. N., Skeie, R. B., Smith, C. J., Smith, S., Tanaka, K., Tsutsui, J., and Xie, Z.: Reduced Complexity Model Intercomparison Project

Phase 1: introduction and evaluation of global-mean temperature response, Geosci. Model Dev., 13, 5175-5190, 10.5194/gmd-13-5175-2020, 2020.
Norris, J., Hall, A., Thackeray, C. W., Chen, D., and Madakumbura, G. D.: Evaluating Hydrologic Sensitivity in CMIP6 Models: Anthropogenic Forcing versus ENSO, Journal of Climate, 35, 6955-6968, https://doi.org/10.1175/JCLI-D-21-0842.1, 2022.
Persad, G., Samset, B. H., Wilcox, L. J., Allen, R. J., Bollasina, M. A., Booth, B. B. B., Bonfils, C., Crocker, T., Joshi, M., Lund, M. T., Marvel, K., Merikanto, J., Nordling, K., Undorf, S., van Vuuren, D. P., Westervelt, D. M., and Zhao, A.: Rapidly evolving aerosol emissions are a dangerous omission from near-term climate risk assessments, Environmental Research: Climate, 2, 032001, 10.1088/2752-5295/acd6af, 2023.
Persad, G. G., and Caldeira, K.: Divergent global-scale temperature effects from identical aerosols emitted in different regions, Nature Communications, 9, 3289, 10.1038/s41467-018-05838-6, 2018.
Platnick, S., and Twomey, S.: Remote sensing the susceptibility of cloud albedo to changes in drop concentration, Atmospheric Research, 34, 85-98, https://doi.org/10.1016/0169-8095(94)90082-5, 1994.
Popp, T., De Leeuw, G., Bingen, C., Brühl, C., Capelle, V., Chedin, A., Clarisse, L., Dubovik, O., Grainger, R., Griesfeller, J., Heckel, A., Kinne, S., Klüser, L., Kosmale, M., Kolmonen, P., Lelli, L., Litvinov, P., Mei, L., North, P., Pinnock, S., Povey, A., Robert, C., Schulz, M., Sogacheva, L., Stebel, K., Stein Zweers, D., Thomas, G., Tilstra, L. G., Vandenbussche, S., Veefkind, P., Vountas, M., and Xue, Y.: Development, Production and Evaluation of Aerosol Climate Data Records from European Satellite Observations (Aerosol_cci), Remote Sensing, 8, 421, 2016.
Recchia, L. G., and Lucarini, V.: Modelling the effect of aerosol and greenhouse gas forcing on the South Asian and East Asian monsoons with an intermediate-complexity climate model, Earth Syst. Dynam., 14, 697-722, 10.5194/esd-14-697-2023, 2023.
Riahi, K., Rao, S., Krey, V., Cho, C., Chirkov, V., Fischer, G., Kindermann, G., Nakicenovic, N., and Rafaj, P.: RCP 8.5—A scenario of comparatively high greenhouse gas emissions, Climatic Change, 109, 33, 10.1007/s10584-011-0149-y, 2011.
Salzmann, M., Weser, H., and Cherian, R.: Robust response of Asian summer monsoon to anthropogenic aerosols in CMIP5 models, Journal of Geophysical Research: Atmospheres, 119, 11,321-311,337, https://doi.org/10.1002/2014JD021783, 2014.
Samset, B. H., Myhre, G., Forster, P. M., Hodnebrog, Ø., Andrews, T., Faluvegi, G., Fläschner, D., Kasoar, M., Kharin, V., Kirkevåg, A., Lamarque, J. F., Olivié, D., Richardson, T., Shindell, D., Shine, K. P., Takemura, T., and Voulgarakis, A.: Fast and slow precipitation responses to individual climate forcers: A PDRMIP multimodel study, Geophysical Research Letters, 43, 2782-2791, 10.1002/2016GL068064, 2016.
Samset, B. H., Myhre, G., Forster, P. M., Hodnebrog, Ø., Andrews, T., Boucher, O., Faluvegi, G., Fläschner, D., Kasoar, M., Kharin, V., Kirkevåg, A., Lamarque, J. F., Olivié, D., Richardson, T. B., Shindell, D., Takemura, T., and Voulgarakis, A.: Weak hydrological sensitivity to temperature change over land, independent of climate forcing, npj Climate and Atmospheric Science, 1, 20173, 10.1038/s41612-017-0005-5, 2018a.
Samset, B. H., Sand, M., Smith, C. J., Bauer, S. E., Forster, P. M., Fuglestvedt, J. S., Osprey, S., and Schleussner, C. F.: Climate Impacts From a Removal of Anthropogenic Aerosol Emissions, Geophysical Research Letters, 45, 1020-1029, doi:10.1002/2017GL076079, 2018b.
Samset, B. H., Lund, M. T., Bollasina, M., Myhre, G., and Wilcox, L.: Emerging Asian aerosol patterns, Nature Geoscience, 12, 582-584, 10.1038/s41561-019-0424-5, 2019.
Song, F., Zhou, T., and Qian, Y.: Responses of East Asian summer monsoon to natural and anthropogenic forcings in the 17 latest CMIP5 models, Geophysical Research Letters, 41, 596-603, https://doi.org/10.1002/2013GL058705, 2014.
Sperber, K. R., Annamalai, H., Kang, I. S., Kitoh, A., Moise, A., Turner, A., Wang, B., and Zhou, T.: The Asian summer monsoon: an intercomparison of CMIP5 vs. CMIP3 simulations of the late 20th century, Climate Dynamics, 41, 2711-2744, 10.1007/s00382-012-1607-6, 2013.

951 Tebaldi, C., Debeire, K., Eyring, V., Fischer, E., Fyfe, J., Friedlingstein, P., Knutti, R., Lowe,
952 J., O'Neill, B., Sanderson, B., van Vuuren, D., Riahi, K., Meinshausen, M., Nicholls, Z.,
953 Tokarska, K. B., Hurtt, G., Kriegler, E., Lamarque, J. F., Meehl, G., Moss, R., Bauer, S. E.,
954 Boucher, O., Brovkin, V., Byun, Y. H., Dix, M., Gualdi, S., Guo, H., John, J. G., Kharin, S.,
955 Kim, Y., Koshiro, T., Ma, L., Olivié, D., Panickal, S., Qiao, F., Rong, X., Rosenbloom, N.,
956 Schupfner, M., Séférian, R., Sellar, A., Semmler, T., Shi, X., Song, Z., Steger, C., Stouffer,
957 R., Swart, N., Tachiiri, K., Tang, Q., Tatebe, H., Voldoire, A., Volodin, E., Wyser, K., Xin, X.,
958 Yang, S., Yu, Y., and Ziehn, T.: Climate model projections from the Scenario Model
959 Intercomparison Project (ScenarioMIP) of CMIP6, Earth Syst. Dynam., 12, 253-293,
960 10.5194/esd-12-253-2021, 2021.
961 Tian, F., Dong, B., Robson, J., and Sutton, R.: Forced decadal changes in the East Asian
962 summer monsoon: the roles of greenhouse gases and anthropogenic aerosols, Climate
963 Dynamics, 51, 3699-3715, 10.1007/s00382-018-4105-7, 2018.
964 Wang, Z., Lin, L., Xu, Y., Che, H., Zhang, X., Zhang, H., Dong, W., Wang, C., Gui, K., and
965 Xie, B.: Incorrect Asian aerosols affecting the attribution and projection of regional climate
966 change in CMIP6 models, npj Climate and Atmospheric Science, 4, 2, 10.1038/s41612-020-
967 00159-2, 2021.
968 Webb, D. J.: An ocean model code for array processor computers, Computers &
969 Geosciences, 22, 569-578, https://doi.org/10.1016/0098-3004(95)00133-6, 1996.
970 Westervelt, D. M., Conley, A. J., Fiore, A. M., Lamarque, J. F., Shindell, D. T., Previdi, M.,
971 Mascioli, N. R., Faluvegi, G., Correa, G., and Horowitz, L. W.: Connecting regional aerosol
972 emissions reductions to local and remote precipitation responses, Atmos. Chem. Phys., 18,
973 12461-12475, 10.5194/acp-18-12461-2018, 2018.
974 Wilcox, L. J., Dunstone, N., Lewinschal, A., Bollasina, M., Ekman, A. M. L., and Highwood, E.
975 J.: Mechanisms for a remote response to Asian anthropogenic aerosol in boreal winter,
976 Atmos. Chem. Phys., 19, 9081-9095, 10.5194/acp-19-9081-2019, 2019.
977 Wilcox, L. J., Liu, Z., Samset, B. H., Hawkins, E., Lund, M. T., Nordling, K., Undorf, S.,
978 Bollasina, M., Ekman, A. M. L., Krishnan, S., Merikanto, J., and Turner, A. G.: Accelerated
979 increases in global and Asian summer monsoon precipitation from future aerosol reductions,
980 Atmos. Chem. Phys. Discuss., 2020, 1-30, 10.5194/acp-2019-1188, 2020.
981 Williams, A. I. L., Stier, P., Dagan, G., and Watson-Parris, D.: Strong control of effective
982 radiative forcing by the spatial pattern of absorbing aerosol, Nature Climate Change, 12, 735-
983 742, 10.1038/s41558-022-01415-4, 2022.
984 Xian, P., Reid, J. S., Ades, M., Benedettie, A., Colarco, P. R., da Silva, A., Eck, T. F.,
985 Flemming, J., Hyer, E. J., Kipling, Z., Rémy, S., Sekiyama, T. T., Tanaka, T., Yumimoto, K.,
986 and Zhang, J.: Intercomparison of Aerosol Optical Depths from four reanalyses and their
987 multi-reanalysis-consensus, EGUsphere, 2023, 1-35, 10.5194/egusphere-2023-2354, 2023.
988 Xie, X., Myhre, G., Liu, X., Li, X., Shi, Z., Wang, H., Kirkevåg, A., Lamarque, J. F., Shindell,
989 D., Takemura, T., and Liu, Y.: Distinct responses of Asian summer monsoon to black carbon
990 aerosols and greenhouse gases, Atmos. Chem. Phys., 20, 11823-11839, 10.5194/acp-20-
991 11823-2020, 2020.
992 Xie, X., Myhre, G., Shindell, D., Faluvegi, G., Takemura, T., Voulgarakis, A., Shi, Z., Li, X.,
993 Xie, X., Liu, H., Liu, X., and Liu, Y.: Anthropogenic sulfate aerosol pollution in South and East
994 Asia induces increased summer precipitation over arid Central Asia, Communications Earth
995 & Environment, 3, 328, 10.1038/s43247-022-00660-x, 2022.
996 Zelinka, M. D., Andrews, T., Forster, P. M., and Taylor, K. E.: Quantifying components of
997 aerosol-cloud-radiation interactions in climate models, Journal of Geophysical Research:
998 Atmospheres, 119, 7599-7615, 10.1002/2014JD021710, 2014.
999 Zelinka, M. D., Smith, C. J., Qin, Y., and Taylor, K. E.: Comparison of methods to estimate
1000 aerosol effective radiative forcings in climate models, Atmos. Chem. Phys., 23, 8879-8898,
1001 10.5194/acp-23-8879-2023, 2023.
1002 Zhang, X. Y., Wang, Y. Q., Niu, T., Zhang, X. C., Gong, S. L., Zhang, Y. M., and Sun, J. Y.:
1003 Atmospheric aerosol compositions in China: spatial/temporal variability, chemical signature,
1004 regional haze distribution and comparisons with global aerosols, Atmos. Chem. Phys., 12,
1005 779-799, 10.5194/acp-12-779-2012, 2012.

1006